Enhanced Signal-to-Noise in Photodetector and DNA-aptamer-based Sensor with a Graphene FET-like Structure

BY

YI LAN
B.S., National Tsing Hua University for Material Science Engineering, 2011

THESIS

Submitted as partial fulfillment of the requirements
for the degree of Doctor of Philosophy in Electrical and Computer Engineering
in the Graduate College of the
University of Illinois at Chicago, 2016

Chicago, Illinois

Defense Committee:

Michael Stroscio, Chair and Advisor
Mitra Dutta
Junxia Shi
Ning Jin
Seyoung An, Nanotechnology Core Facility at University of Illinois at Chicago

ACKNOWLEDGMENTS

First, thanks to my Ph.D. advisor Professor Stroscio and his wife, Professor Dutta that they helped me a lot not only in the research field, also took care of me for life in Chicago. They are both brilliant scholars and educators.

Second, thanks to Professor James Lin for teaching me patiently how to be a good TA and deal with students. He's the first professor I worked with for my TA job. He's also pretty talkative in many other fields, music, history, geography, foods, etc., which always made me having new perspective to the world.

Third, thanks to Professor Ning Jin for guiding me as an elder brother. Thanks to Dr. Seyoung An for helping me with the training in NCF. Thanks to Professor Lucy Shi for excellent cooperation with her lab.

Fourth, thanks to Yung Yu Wang for sending me a bunch of graphene-FET samples from UCI. Also, he treats me as a little sister bringing me to all kinds of good restaurants in Kaohsiung in the winter vacation 2015.

Fifth, thanks to everyone in our group: Nanzhu Zhang, Choi Min, Sidra Farid, Xenia Meshik, Ke Xu, Souvik Mukherjee, and Debopam Dutta. Our group is so joyful all because of you guys. Also, thanks to Guan-Lin Su, Ran Zhang, and Ting-Ya Chiu for hanging out with me all the time. They are my best friends here!

The most important people I want to thanks to are my family, including my mom, my sister, and my grandparents. They are always on my side, and taking with me through facetime every day.

YL

CONTRIBUTION OF AUTHORS

Chapter 1 and Chapter 2 are partly published in © 2014 IEEE which having co-authors Nanzhu Zhang and my advisers. Howerer, I didn't contain any graph published in my thesis, and I didn't put any Nanzhu Zhang's work in my thesis. In another words, the part done by Nanzhu Zhang in the paper we published together is not shown in my thesis. Chapter 3 is totally unpublished. Chapter 4 is partly published in © 2015 IEEE which having co-authors Chenjie and my advisers. But in my thesis, only Figure 22 is done by Chenjie. And that figure is an unpublished one as well. Chapter 5 and Chapter 6 haven't been published yet. In Chapter 6, the FET PDMS-graphene structures was fabricated at the University of California at Irvine under the direction of Prof. Peter Burke. But I didn't put any of their studies in my thesis.

TABLE OF CONTENTS

CHAPTER **PAGE**

TABLE OF CONTENTS (continued)

CHAPTER **PAGE**

TABLE OF CONTENTS (continued)

CHAPTER **PAGE**

LIST OF TABLES

TABLE **PAGE**

LIST OF FIGURES

FIGURE **PAGE**

LIST OF FIGURES (Continued)

FIGURE **PAGE**

LIST OF ABBREVIATIONS

CB	Conduction Band
VB	Valence Band
QW	Quantum well
IgE	Immunoglobulin E
FET	field-effect-transistor
SELEX	Systematic Evolution of Ligands by Exponential enrichment
TBA	thrombin binding aptamer
PDMS	Polydimethylsiloxane
DI water	deionized water
DMF	Dimethylformamide
PBS	Phosphate-buffered saline
BSA	Bovine serum albumin

SUMMARY

In the enhanced signal-to-noise in photodetectors part, we design a photodetector absorbing two photon and emitting one phonon. According to Richardson's thermionic emission theory, our design can efficiently reduce the noise.

Then, we do the simulation for the design in several sets of different materials to show the practicability of it. In Chapter 2, $Ga_{1-x}Al_xAs$, $In_{1-y}Ga_yAs$, and $In_{1-x}Al_xAs/InP$ designs are elaborated.

In Chapter 3 and 4, interface phonon properties is brought out. Phonon dispersion curve of 22 phonon modes existing in this design is calculated for this design, and the interface phonon potential curve along the structure for each mode is plotted. Therefore, we are able to apply them on the calculation of phonon transfer efficiency in Chapter 5, figuring out a pretty fast transferring time is guaranteed in our structure.

For another part of my research - DNA-aptamer-based sensors with graphene FET-like structure, the conductivity of the graphene FET sensor changing with Immunoglobulin E aptamer and target is well described. This sensor can also apply on different aptamers and targets which is prospective in biological and medical aspect.

CHAPTER 1

INTRODUCTION OF ENHANCED SIGNAL-TO-NOISE IN PHOTODETECTOR

A quantum well photodetector is designed for reducing signal-to-noise in this research. [7] We use a single-double quantum well structure to proceed a sequence of events: absorbing a photon, emitting a phonon, and absorbing a photon having the same wavelength as the first one. Even though this process needs two absorbed photons to produce one electron out of the apparatus for detection, a demonstration that it dramatically reduces the noise is based on rapid phonon-assisted transitions along with phonon quantum engineering and nanoscale electron states.

1.1 Single-Double quantum well design

Based on the ideas we discussed previously [1-3] about heterosturcture lasers, which lead to extremely large emphasis on the optical gain of quantum-well-based lasers, that examines dramatic emphasis on photodetectivity in QW-based photodetectors in the earliest known embodiment which is able to detect photons in the frequency over a wide range. Herein, we design a triple quantum well structure with one single well on the left side, and one double well on the right side as shown in **Figure 1**. In the first quantum well, the electron absorbing one photon jumping from the ground state of the single well E_1 to the first excited state of the single well E_3.

---

[0]Parts of this thesis were reproduced with permission from © 2014 IEEE

Then, the electron tunnels through the barrier to the double well as a result of interface-phonon assisted tunneling. In the double well, E_2 and $E_{2'}$ is the splitting of the ground state, and E_4 and $E_{4'}$ is the splitting of the first excited state. In our design, $E_{2'}$ and E_3 are degenerate and phonon emission is enhanced as a result of an increased matrix element. After emitting one phonon, the electron falls to E_2 state. In the final process, the electron absorbs another photon having the same wavelength, which we are detecting, as the first photon absorption, and jumps to E_4. The relationship between energy levels in this design can be sum up as following:

$$\begin{aligned} E_3 &= E_{2'} \\ E_3 - E_1 &= E_{4'} - E_2 = E_{Photon} \\ E_{2'} - E_2 &= E_{Phonon} \end{aligned} \tag{1.1}$$

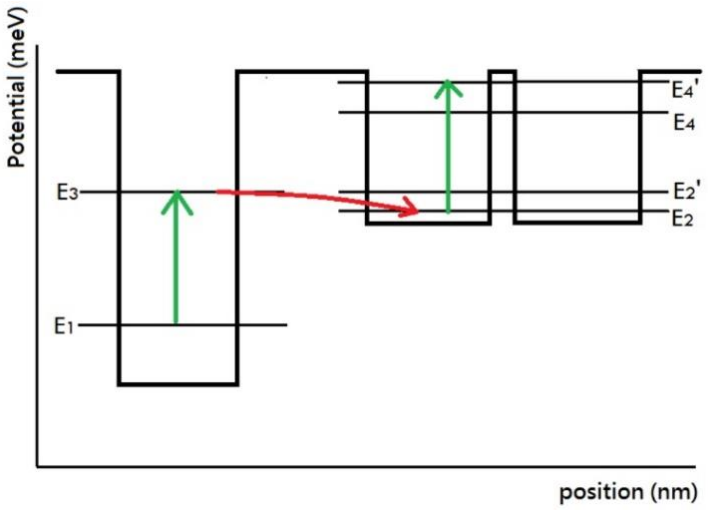

Figure 1. Single-Double well Design.

1.2 Signal-to-Noise Enhancement

According to Richardson's formula,

$$\frac{I_{sn,E_1}}{I_{sn,E_2}} = \frac{e^{-\frac{E_4-E_1}{kT}}}{e^{-\frac{E_4-E_2}{kT}}} = \frac{e^{-\frac{2E_{photon}-E_{phonon}}{kT}}}{e^{-\frac{E_{photon}}{kT}}} = e^{-\frac{E_{photon}-E_{phonon}}{kT}} \quad (1.2)$$

The noise current, $I_{sn,E1}$, produced by the energy changing from E_1 to E_4 with two photon absorption and one phonon emission compares to the noise current, $I_{sn,E2}$, having energy changing of one phonon (from E_2 to E_4). Referring to **Figure 2**, it is obvious to see the noise is dramatically reduced.

For example if $\frac{E_{photon}-E_{phonon}}{kT} = 6.9$, and $kT = 0.0257\ eV$ at T = 298 K, a dramatic 1.0078×10^{-3} reduction can be realized for $E_{photon} = 211.19\ eV$ and $E_{phonon} = 33.79\ eV$.

We can say that in our design, signal-to-noise in the photodetector is well enhanced.

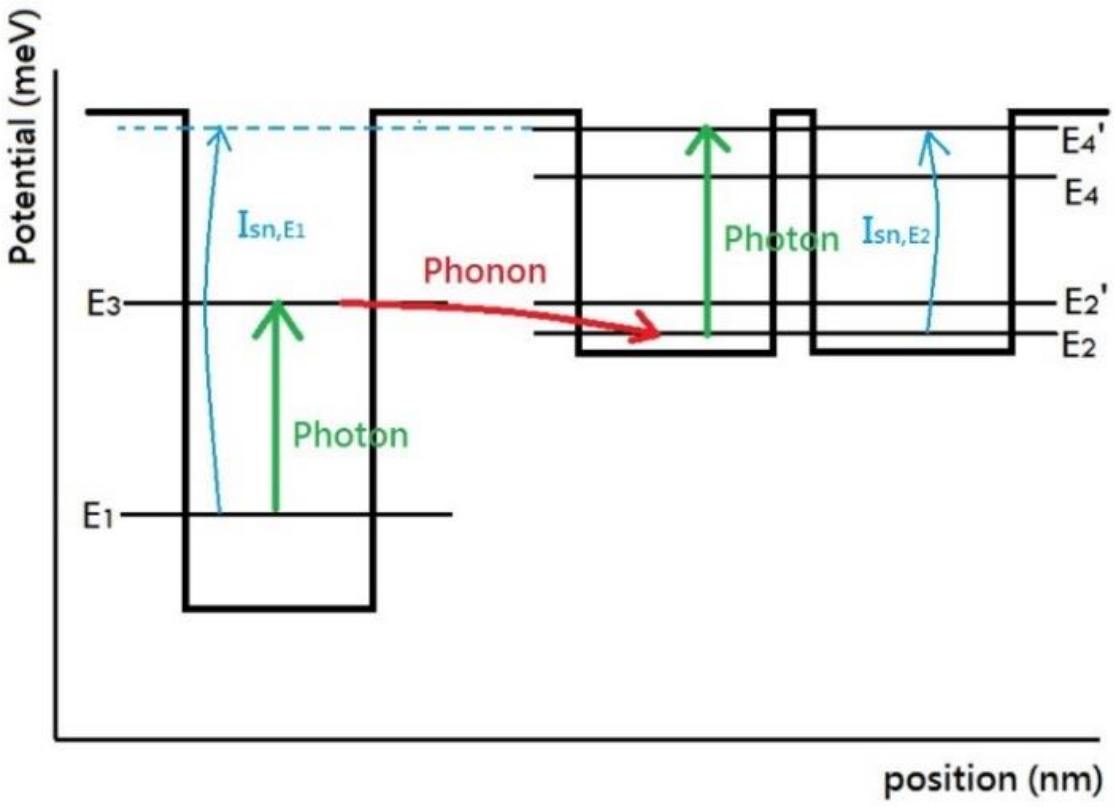

Figure 2. Illustration of thermal ionization current.

1.3 Transfer Efficiency

According to the Fermi's Golden Rule [1], we can consider the transfer efficiency.

$$\frac{1}{\tau_i} = \frac{2\pi}{\hbar}\sum_f \left|\langle f|\tilde{H}|i\rangle\right|^2 \delta(E_f - E_i) \tag{1.3}$$

where τ_i is the transfer efficiency, f is the final state wave function, i is the initial state wave function, and $\tilde{H}$ is the photon/phonon interaction potential.

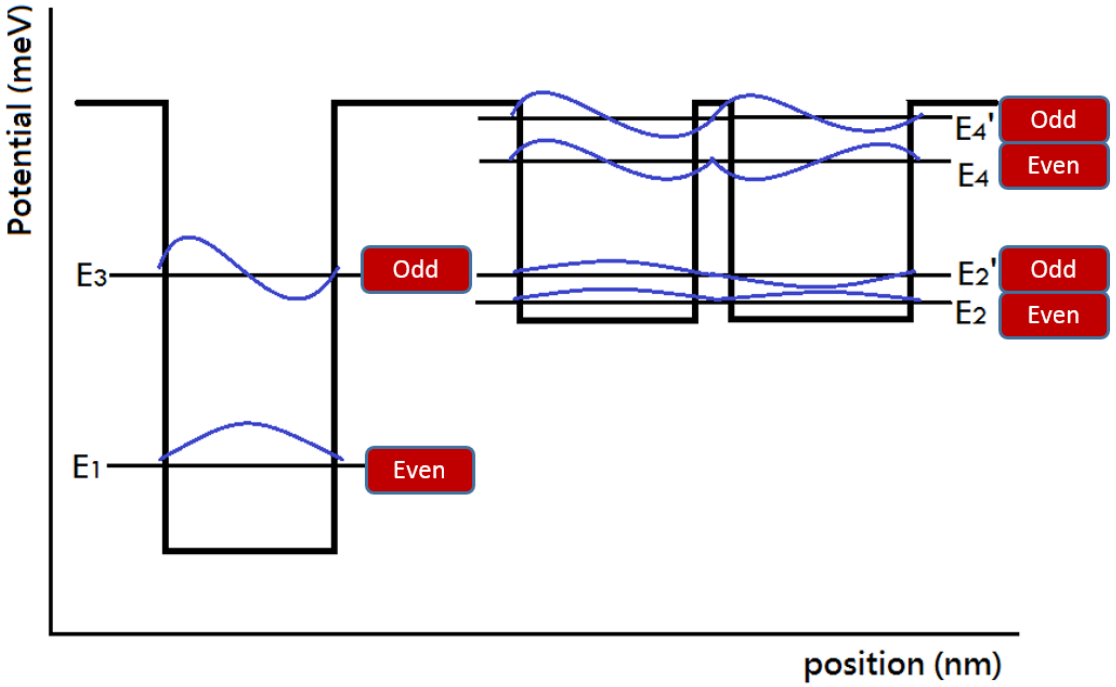

Figure 3. Signal-to-noise ratio enhanced by Richardson formula.

We would like to have the matrix elements for phonon assisted transition be as large as possible. The situation depends on the symmetric of the initial and final electron states as well as the electron-phonon interaction potential.

From **Figure 3**, it can be easily seen that the wave functions corresponding to E_1 E_2 E_4 are even, and those corresponding to E_3 $E_{2'}$ $E_{4'}$ are odd.

Therefore, E_1 to E_3, and E_2 to $E_{4'}$ are selected as the photon absorbing levels, and the first double well energy state splitting of $E_{2'}$ and E_2 are picked as phonon emitting levels.

1.4 Model Simulation

The Schrödinger equation with effective mass mismatch at heterojunctions is used for

calculating the energy levels.

$$-\frac{\hbar^2}{2m_1^*}\frac{\partial^2}{\partial z^2}\varphi_1(z)+V_1\varphi_1(z)=E_1\varphi_1(z) \quad \text{when } z \le 0$$

$$-\frac{\hbar^2}{2m_2^*}\frac{\partial^2}{\partial z^2}\varphi_2(z)=E_1\varphi_2(z) \quad \text{when } 0 \le z \le z_1 \tag{1.4}$$

$$-\frac{\hbar^2}{2m_1^*}\frac{\partial^2}{\partial z^2}\varphi_3(z)+V_1\varphi_3(z)=E_1\varphi_3(z) \quad \text{when } z_1 \le z \le z_2$$

Equation (1.4) is the Schrödinger equations for the single well, where m_i^* is the effective mass, $\varphi_i(z)$ is the potential curve along the z direction, and V_1 is the conduction band energy level difference between the barrier and well for the single well, and E_1 will be the possible energy levels that can be solved in the single well.

$$-\frac{\hbar^2}{2m_1^*}\frac{\partial^2}{\partial z^2}\varphi_3(z)+V_1\varphi_3(z)=E_2\varphi_3(z) \quad \text{when } z_1 \le z \le z_2$$

$$-\frac{\hbar^2}{2m_3^*}\frac{\partial^2}{\partial z^2}\varphi_4(z)+(V_1-V_2)\varphi_4(z)=E_2\varphi_4(z) \quad \text{when } z_2 \le z \le z_3$$

$$-\frac{\hbar^2}{2m_1^*}\frac{\partial^2}{\partial z^2}\varphi_5(z)+V_1\varphi_5(z)=E_2\varphi_5(z) \quad \text{when } z_3 \le z \le z_4 \tag{1.5}$$

$$-\frac{\hbar^2}{2m_3^*}\frac{\partial^2}{\partial z^2}\varphi_6(z)+(V_1-V_2)\varphi_6(z)=E_2\varphi_6(z) \quad \text{when } z_4 \le z \le z_5$$

$$-\frac{\hbar^2}{2m_1^*}\frac{\partial^2}{\partial z^2}\varphi_7(z)+V_1\varphi_7(z)=E_2\varphi_7(z) \quad \text{when } z_5 \le z$$

Equation (1.5) represents the Schrödinger equations for the double well, where m_i^* is the electron effective mass, $\varphi_i(z)$ is the potential curve along z direction, and V_2 is the conduction band energy level difference between the barrier and well for the single well, and E_2 will be the possible energy levels that can be solved in this double well.

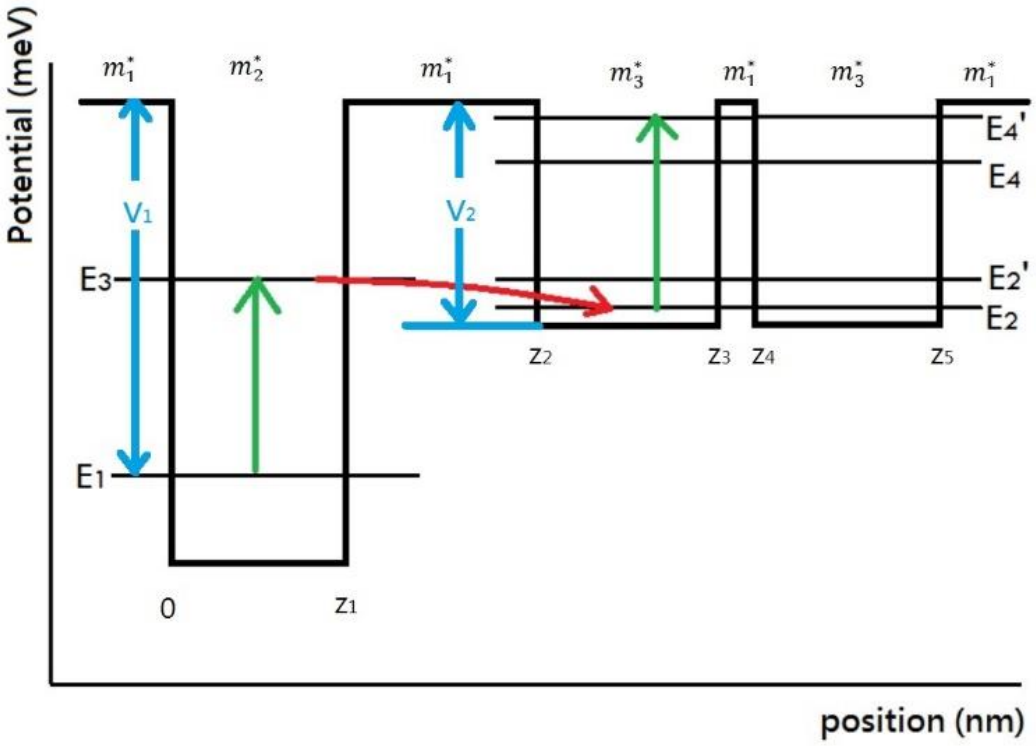

Figure 4. Corresponding parameters for the calculation of energy levels.

Solving the boundary condition, we can try to fit the energy levels as needed. The energy levels should follow the relationship as mentioned in section 1.1: 1) E_3 equals $E_{2'}$, and 2) the energy difference between E_3 and E_2, which is also splitting of the ground state in the double quantum well, equals to one phonon energy. 3) The energy difference

between E_3 and E_1, and the energy difference between $E_{4'}$ and E_2 should be the same, and also equal to one photon energy.

The interface phonon modes of our structure will be calculated in Chapter 3. One of the phonon modes needs to have an energy such that $E_{phonon} = E_{2'}-E_2$ in our structure.

CHAPTER 2

SINGLE-DOUBLE QUANTUM WELL SIMULATION

In Chapter 1, a design of single-double quantum well was described that leads to an enhanced signal-to-noise photodetector. We would like to have more kinds of material designs in our single-double well enhanced signal-to-noise photodetector. Changing the material of our design can form different potentials for the depth of wells, and leads to detect different wavelength of photons and applications [31-33]. In this Chapter, we are doing three simulations in familiar materials that easily obtained.

2.1 $Ga_{1-x}Al_xAs$ Design

2.1.1 Parameters for $Ga_{1-x}Al_xAs$

This section deals with the parameters we need to model our new device. These parameters include the discontinuity of conduction band energy for $Ga_{1-x}Al_xAs$ that having different concentration of x, and the corresponding electron effective mass.

As we know, the band gap energy for $Ga_{1-x}Al_xAs$ is:

$$E_g = (1.426 + 1.247x)\ eV \tag{2.1}$$

---

[0]Parts of this thesis were reproduced with permission from © 2014 IEEE

The band alignment is 33% of the total discontinuity in valence band, which means:

$$\Delta V_{VB} = 0.33 \tag{2.2}$$

$$\Delta V_{CB} = 0.67 \tag{2.3}$$

The electron effective mass is given by,

$$m^* = (0.067 + 0.083x)m_0 \tag{2.4}$$

where $m_0 = 9.10938215 \times 10^{-31}$.

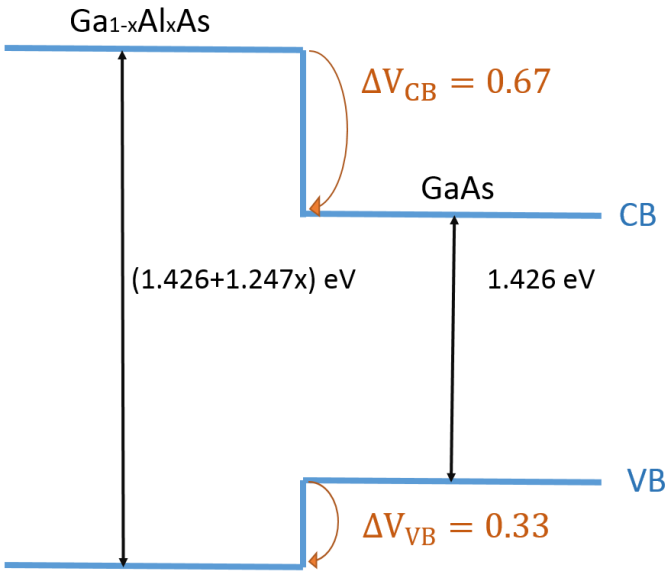

Figure 5. Band gap energy discontinuity for $Ga_{1-x}Al_xAs$.

2.1.2 Structure designed for $Ga_{1-x}Al_xAs$

Using the property of the band discontinuity of $Ga_{1-x}Al_xAs$, quantum wells are easily formed. We can change the concentration of GaAs and AlAs by adjusting the value of x, and get the quantum well depth wanted. A design shown as **Figure 6** can bring out the single-double well quantum wells structure.

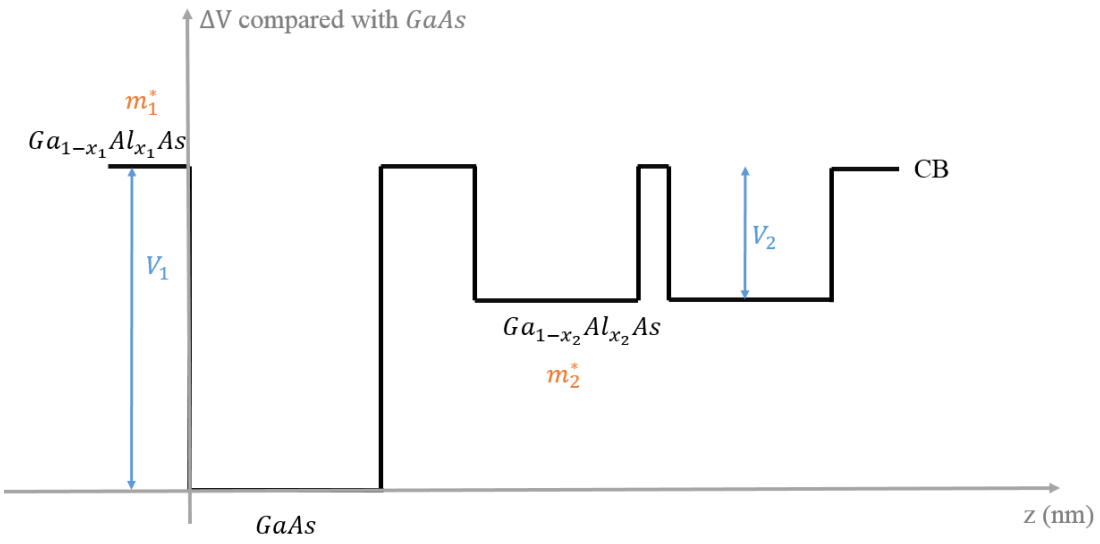

Figure 6. Basic design of single-double quantum well in $Ga_{1-x}Al_xAs$ material.

For the voltage level changing compared with GaAs of wells and barriers in Figure 6,

$$V_1 = 1.247x_1 \times 0.67 \tag{2.5}$$

$$V_1 - V_2 = 1.247x_2 \times 0.67 \tag{2.6}$$

The corresponding electron effective mass are,

$$m_1^* = (0.067 + 0.083x_1) \times m_0 \tag{2.7}$$

$$m_2^* = (0.067 + 0.083x_2) \times m_0 \tag{2.8}$$

where, $m_{GaAs}^* = 0.067m_0$.

2.1.3 Simulation of $Ga_{1-x}Al_xAs$ design

Appendix A describes a Matlab code written for calculating the energy states in the single-double quantum well design with GaAlAs material. The Schrödinger equations based on the previously-discussed results are:

$$-\frac{\hbar^2}{2m_0(0.067 + 0.083x_1)}\frac{\partial^2}{\partial z^2}\varphi_1(z) + (1.247x_1 \times 0.67)\varphi_1(z) = E\varphi_1(z)$$

when $z \leq 0$

$$-\frac{\hbar^2}{2 \times 0.067m_0}\frac{\partial^2}{\partial z^2}\varphi_2(z) = E\varphi_2(z)$$

when $0 \leq z \leq z_1$ (2.9)

$$-\frac{\hbar^2}{2m_0(0.067 + 0.083x_1)}\frac{\partial^2}{\partial z^2}\varphi_3(z) + (1.247x_1 \times 0.67)\varphi_3(z) = E\varphi_3(z)$$

when $z_1 \leq z \leq z_2$

$$-\frac{\hbar^2}{2m_0.067 + 0.083x_2)}\frac{\partial^2}{\partial z^2}\varphi_4(z) + (1.247x_2 \times 0.67)\varphi_4(z) = E\varphi_4(z)$$

when $z_2 \leq z \leq z_3$

$$-\frac{\hbar^2}{2m_0(0.067+0.083x_1)}\frac{\partial^2}{\partial z^2}\varphi_5(z)+(1.247x_1\times 0.67)\varphi_5(z)=E\varphi_5(z)$$

when $z_3 \le z \le z_4$

$$-\frac{\hbar^2}{2m_0(0.067+0.083x_2)}\frac{\partial^2}{\partial z^2}\varphi_6(z)+(1.247x_2\times 0.67)\varphi_6(z)=E\varphi_6(z)$$

when $z_4 \le z \le z_5$

$$-\frac{\hbar^2}{2m_0(0.067+0.083x_1)}\frac{\partial^2}{\partial z^2}\varphi_7(z)+(1.247x_1\times 0.67)\varphi_7(z)=E\varphi_7(z)$$

when $z_5 \le z$

where $\hbar = 1.054571628\times 10^{-34}$, and $m_0 = 9.10938215\times 10^{-31}$.

As shown in Figure 7, we can change the concentration of x_1 and x_2 to change the depth single and double quantum wells which have impact on the energy state levels E_1, E_2, $E_{2'}$, E_3, E_4, and $E_{4'}$. The larger the x is, indicating that the concentration of AlAs increases, the higher the conduction band level will be.

Also, adjusting the thickness of wells and barriers can alter the energy state levels. When the thickness of the well is wider, the energy states goes lower, and also the energy differences between energy states become smaller. For the double well, the thicker the barrier between the double well is, the closer the splitting of the energy states will be.

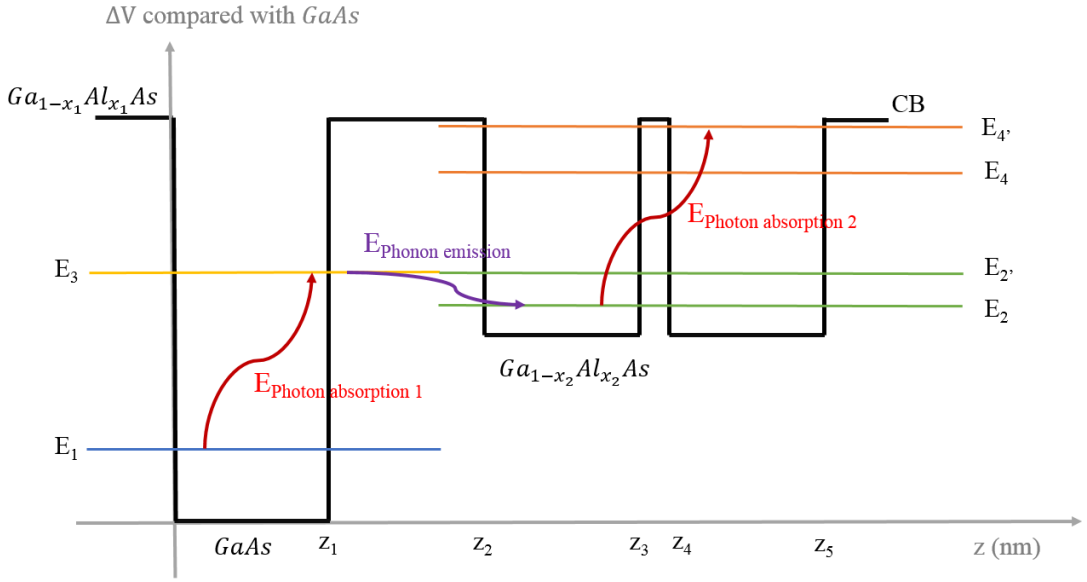

Figure 7. Simulation for single-double quantum well in $Ga_{1-x}Al_xAs$ material.

After many calculations are made, one set of single-double well design parameter for GaAlAs material that optimizes the signal-to-noise in the photodetector is found as shown in Figure 8.

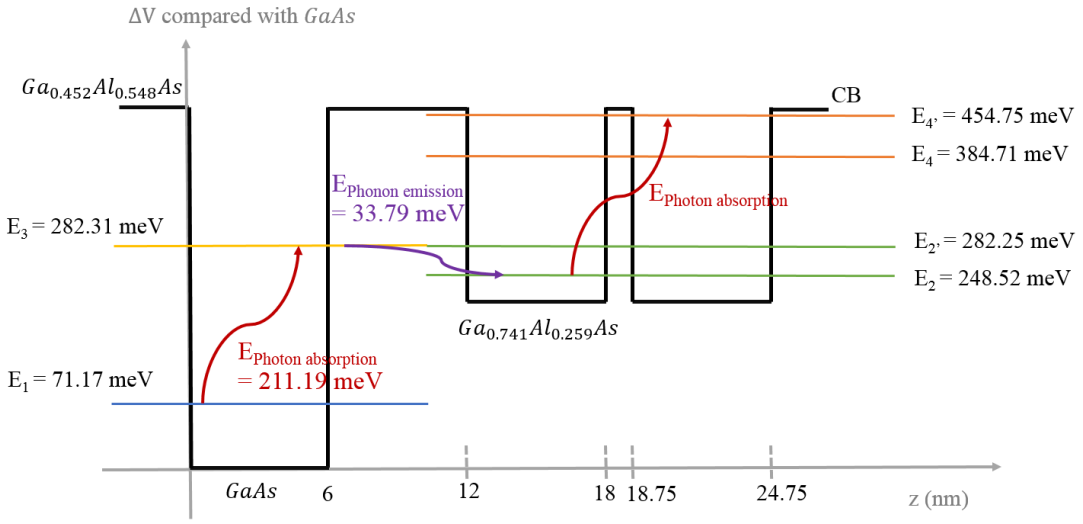

Figure 8. Result of signal-to-noise enhanced photodetector in $Ga_{1-x}Al_xAs$ material.

For the single well, $Ga_{0.452}Al_{0.548}As$ is used as the barrier, and GaAs as the well. The potential of the single well then turns out to be 457.849 meV. For the double well, $Ga_{0.452}Al_{0.548}As$ is still the barrier, both outside the double well and between it, and now we use $Ga_{0.741}Al_{0.259}As$ as the well. A depth of 241.457 meV as potential of the double well is obtained.

In this result, we have the width of single well as 6 nm, and the width of each wells in double well as 6 nm as well. The barrier between the double well is 0.75 nm, and the barrier between single well and double well is 6 nm.

The energy states in single well then turns out to be E_1 = 71.17 meV, and E_3 = 282.31 meV. In the double well, energy states are E_2 = 248.52

meV, $E_{2'}$ = 282.52 meV, E_4 = 384.71 meV, and $E_{4'}$ = 454.75 meV as shown in Figure 8.

The whole process of this signal-to-noise photodetector in this design works as following:

i. From the E_1 state, an electron absorbs one photon energy which equals to 211.19 meV, having wavelength of 5871.49 nm, and jumps to E_3 state.

ii. The electron emits one phonon energy of 33.79 meV, and falls down to the state E_2.

iii. Absorbing another photon with 206.23 meV (wavelength = 6012.70 nm) which having similar energy as the first one, the electron jumps to $E_{4'}$, which is very close to the barrier level of $Ga_{0.452}Al_{0.548}As$, and will be detected.

A range of light source which includes 5871.49 nm and 6012.70 nm will be detected by this detector.

2.2 $In_{1-y}Ga_yAs$ Design

2.2.1 Parameters for $In_{1-y}Ga_yAs$

For $In_{1-y}Ga_yAs$, the need parameters must be specified; the parameters includes the discontinuity of conduction band energy for $In_{1-y}Ga_yAs$ that having different concentration of y, and its electron effective mass.

The total band gap energy discontinuity for $In_{1-x-y}Al_xGa_yAs/AlAs$ is:

$$\Delta V = [2.093x + 0.629y + 0.577x^2 + 0.436y^2 + 1.013xy - 2.0x^2(1 - x - y)]\ eV \quad (2.10)$$

and the band alignment is 47% of the total discontinuity in valence band, which means:

$$\Delta V_{VB} = 0.47 \quad (2.11)$$

$$\Delta V_{CB} = 0.53 \quad (2.12)$$

The electron effective mass for $In_{1-x-y}Al_xGa_yAs/AlAs$ is:

$$m^* = (0.0427 + 0.0685x)m_0 \quad (2.13)$$

where $m_0 = 9.10938215 \times 10^{-31}$.

Therefore, if $x = 0$ is assumed in all the parameters, we can get parameters in $In_{1-y}Ga_yAs/AlAs$ follows:

$$\Delta V' = (0.629y + 0.436y^2)\ eV \quad (2.14)$$

and since $\Delta V_{VB} = 0.47$ and $\Delta V_{CB} = 0.53$, the conduction band discontinuity of $In_{1-y}Ga_yAs/AlAs$ is:

$$\Delta V'' = [(0.629y + 0.436y^2) \times 0.53]\ eV \quad (2.15)$$

Also,

$$m^{*\prime} = 0.0427m_0 \quad (2.16)$$

where $m_0 = 9.10938215 \times 10^{-31}$.

2.2.2 Structure designed for $In_{1-y}Ga_yAs$

Since Figure 9 illustrates the association of parameters of the $In_{1-y}Ga_yAs$ single-double well design and with different regions of the structure.

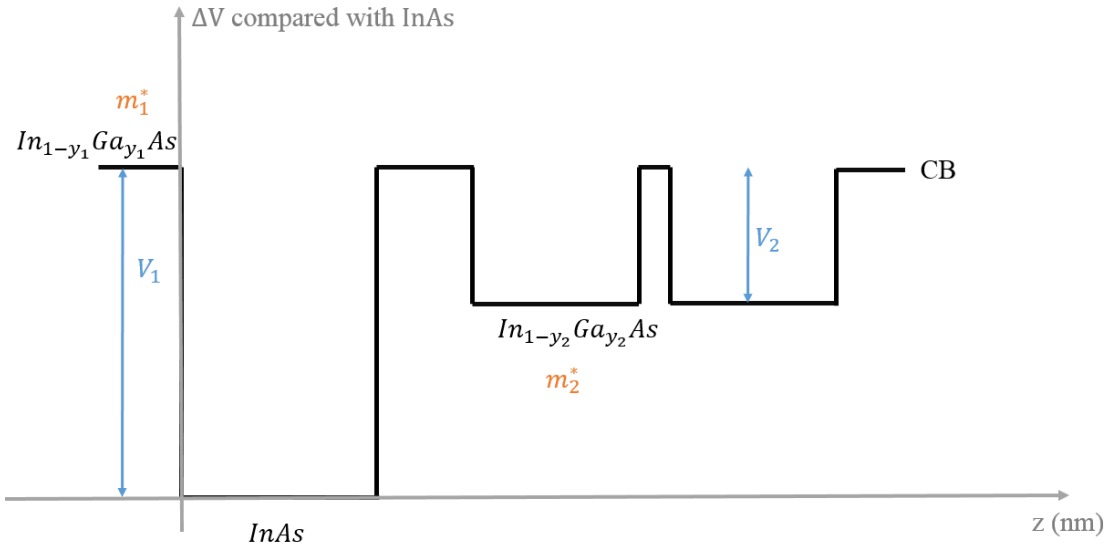

Figure 9. Single-double quantum well design in $In_{1-y}Ga_yAs$ material.

For the voltage level changing compared with InAs of wells and barriers in Figure 9, we have,

$$V_1 = (0.629y_1 + 0.436y_1^2) \times 0.53 \tag{2.17}$$

$$V_1 - V_2 = (0.629y_2 + 0.436y_2^2) \times 0.53 \tag{2.18}$$

and the corresponding electron effective mass are,

$$m_1^* = 0.0427m_0 \tag{2.19}$$

$$m_2^* = 0.0427m_0 \tag{2.20}$$

with $m_{InAs}^* = 0.067m_0$.

2.2.3 Simulation of $In_{1-y}Ga_yAs$ design

The wave equations for the $In_{1-y}Ga_yAs$ single-double quantum well structure can now be described as follows:

$$-\frac{\hbar^2}{2 \times 0.0427m_0}\frac{\partial^2}{\partial z^2}\varphi_1(z) + [(0.629y_1 + 0.436y_1^2) \times 0.53]\varphi_1(z) = E\varphi_1(z)$$

when $z \leq 0$

$$-\frac{\hbar^2}{2 \times 0.0427m_0}\frac{\partial^2}{\partial z^2}\varphi_2(z) = E\varphi_2(z)$$

when $0 \leq z \leq z_1$

$$-\frac{\hbar^2}{2 \times 0.0427m_0}\frac{\partial^2}{\partial z^2}\varphi_3(z) + [(0.629y_1 + 0.436y_1^2) \times 0.53]\varphi_3(z) = E\varphi_3(z) \tag{2.21}$$

when $z_1 \leq z \leq z_2$

$$-\frac{\hbar^2}{2 \times 0.0427m_0}\frac{\partial^2}{\partial z^2}\varphi_4(z) + [(0.629y_2 + 0.436y_2^2) \times 0.53]\varphi_4(z) = E\varphi_4(z)$$

when $z_2 \leq z \leq z_3$

$$-\frac{\hbar^2}{2\times 0.0427m_0}\frac{\partial^2}{\partial z^2}\varphi_5(z)+[(0.629y_1+0.436y_1^2)\times 0.53]\varphi_5(z)$$

$$=E\varphi_5(z)$$

when $z_3 \le z \le z_4$

$$-\frac{\hbar^2}{2\times 0.0427m_0}\frac{\partial^2}{\partial z^2}\varphi_6(z)+[(0.629y_2+0.436y_2^2)\times 0.53]\varphi_6(z)$$

$$=E\varphi_6(z)$$

when $z_4 \le z \le z_5$

$$-\frac{\hbar^2}{2\times 0.0427m_0}\frac{\partial^2}{\partial z^2}\varphi_7(z)+[(0.629y_1+0.436y_1^2)\times 0.53]\varphi_7(z)$$

$$=E\varphi_7(z)$$

when $z_5 \le z$

where $\hbar = 1.054571628\times 10^{-34}$, and $m_0 = 9.10938215\times 10^{-31}$.

Coding them into Matlab, the values y_1, y_2, z_1, z_2, z_3, z_4, and z_5 in the single-double quantum wells design are obtained to ensure the required resonant conditions for the energy states. Figure 10 illustrates the demands for signal-to-noise enhanced photodetector.

In $In_{1-y}Ga_yAs$ design, the larger the y is, which means when the concentration of GaAs is higher, the higher the conduction band level will be.

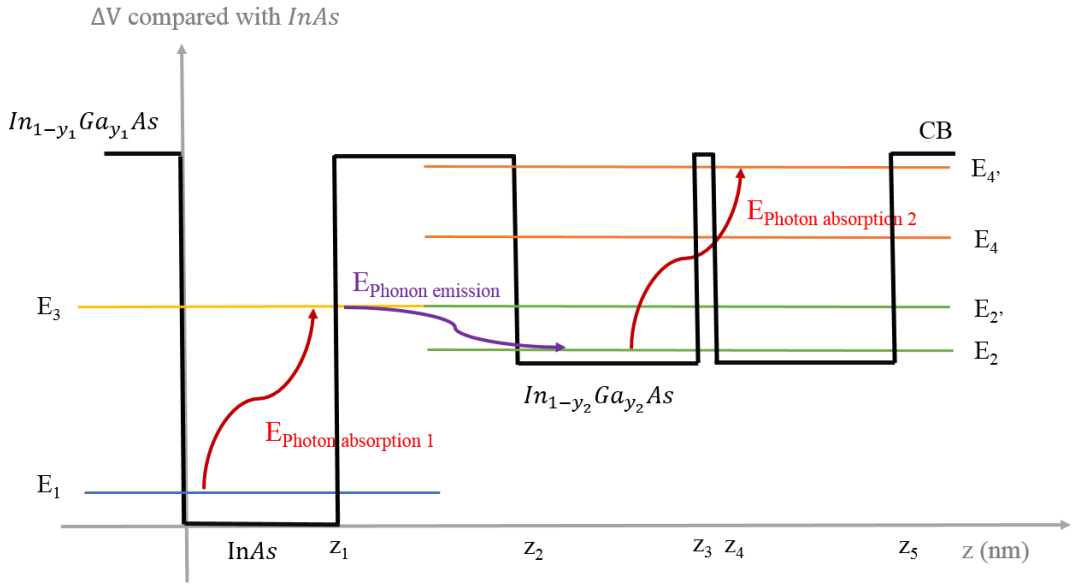

Figure 10. Simulation for Single-Double Quantum Well in $In_{1-y}Ga_yAs$ material.

Figure 11 depicts the optimized structure for the design in InGaAs material based on many calculations performed by adjusting these parameters.

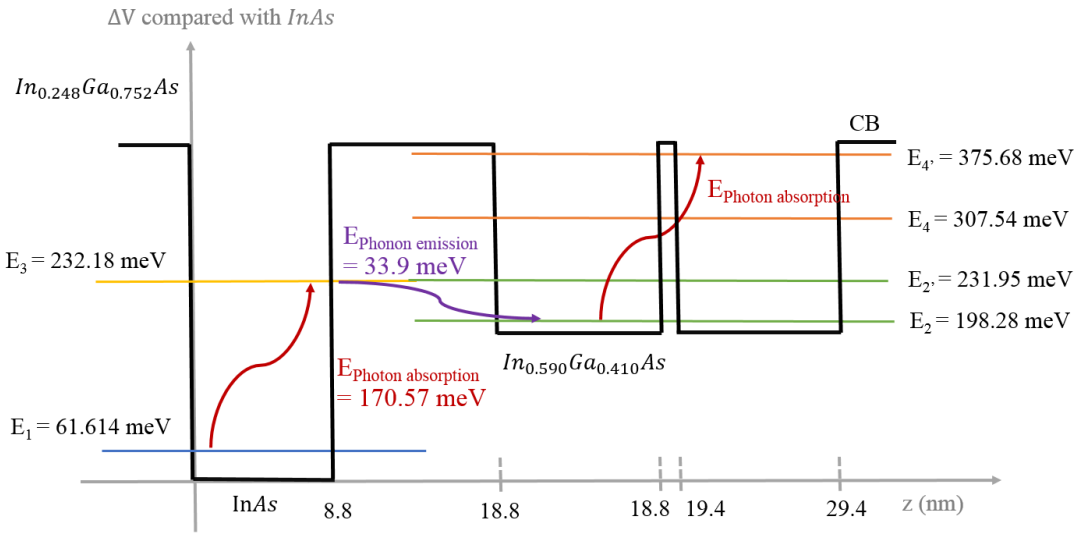

Figure 11. Optimized Signal-to-Noise enhanced photodetector in $In_{1-y}Ga_yAs$ material.

For the single well, $In_{0.248}Ga_{0.752}As$ is used as the barrier, and InAs as the well. The potential of the single well then turns out to be 381.371 meV. For the double well, $In_{0.248}Ga_{0.752}As$ is still the barrier, both outside the double well and between it, and now we use $In_{0.590}Ga_{0.410}As$ as the well. A depth of 205.845 meV as the potential of the double well is obtained.

In this result, we have the width of single well as 8.8 nm, and the width of each well in double well as 10 nm. The barrier between the double well is 0.6 nm, and the barrier between single well and double well is 10 nm.

The energy states in single well then turn out to be E_1 = 61.614 meV, and E_3 = 232.18 meV. In the double well, energy states are E_2 = 198.28

meV, $E_{2'}$ = 231.95 meV, E_4 = 307.54 meV, and $E_{4'}$ = 375.68 meV as shown in Figure 11.

The whole process for this signal-to-noise photodetector with InGaAs material in this design works as following:

i. From E_1 state, an electron absorbs one photon energy which equals to 170.57meV, having wavelength of 7269.74 nm, and transitions to the E_3 state.

ii. The electron emits one phonon energy of 33.9 meV, with wavelength 36578.17 nm, and falls down to the state E_2.

iii. Absorbing another phonon with 177.4 meV (wavelength = 6989.85 nm) which having similar energy as the first one, the electron transitions to $E_{4'}$, which is very close to the barrier level of $In_{0.248}Ga_{0.752}As$, and will be detected.

The photon absorption for the first photon and the second photon having a difference of 4% in energy. Even though, error less than 5% is acceptable in experiment, the light source being detected needs to have a wide band at least from 6989.85 nm to 7269.74 nm in this apparatus.

2.3 $In_{1-x}Al_xAs/InP$ Design

2.3.1 Parameters for $In_{1-x}Al_xAs/InP$

The parameters we need include: the discontinuity of conduction band energy for $In_{1-x}Al_xAs$ that having different concentration of x, the electron effective mass for the corresponding x value, and the conduction band energy

level and electron effective mass of InP.

The total band gap energy discontinuity for $In_{1-x-y}Al_xGa_yAs/AlAs$ is mentioned in the previous part as:

$$\Delta V = [2.093x + 0.629y + 0.577x^2 + 0.436y^2 + 1.013xy - 2.0x^2(1 - x - y)]\ eV \quad (2.22)$$

and the band alignment is 47% of the total discontinuity in valence band, which means:

$$\Delta V_{VB} = 0.47 \quad (2.23)$$

$$\Delta V_{CB} = 0.53 \quad (2.24)$$

The electron effective mass for $In_{1-x-y}Al_xGa_yAs/AlAs$ is:

$$m^* = (0.0427 + 0.0685x)m_0 \quad (2.25)$$

where $m_0 = 9.10938215 \times 10^{-31}$.

Therefore, if $y = 0$ is assumed in all the parameters, we can get parameters for $In_{1-x}Al_xAs/AlAs$ as follows:

The total band discontinuity is:

$$\Delta V' = (2.093x - 1.423x^2 + 2x^3)\ eV \quad (2.26)$$

and since that $\Delta V_{VB} = 0.47$ and $\Delta V_{CB} = 0.53$, the conduction band discontinuity of $In_{1-y}Ga_yAs/AlAs$ is:

$$\Delta V'' = [(2.093x - 1.423x^2 + 2x^3) \times 0.53]\ eV \quad (2.27)$$

Also,

$$m^{*\prime} = (0.0427 + 0.0685x)m_0 \tag{2.28}$$

where $m_0 = 9.10938215 \times 10^{-31}$.

From reference 3, the heterointerface in the InGaAs/InAlAs/InP family is described as follows:

For the conduction band energy level, $In_{0.52}Al_{0.48}As$ is 0.34 eV higher than InP.

From equation 2.27, we can calculate that the conduction band discontinuity of $In_{0.52}Al_{0.48}As$ to AlAs is 0.475921 eV.

Again from equation 2.27, the conduction band discontinuity of InAs to AlAs is 1.4151 eV.

Figure 12 depicts the relevant energy conditions.

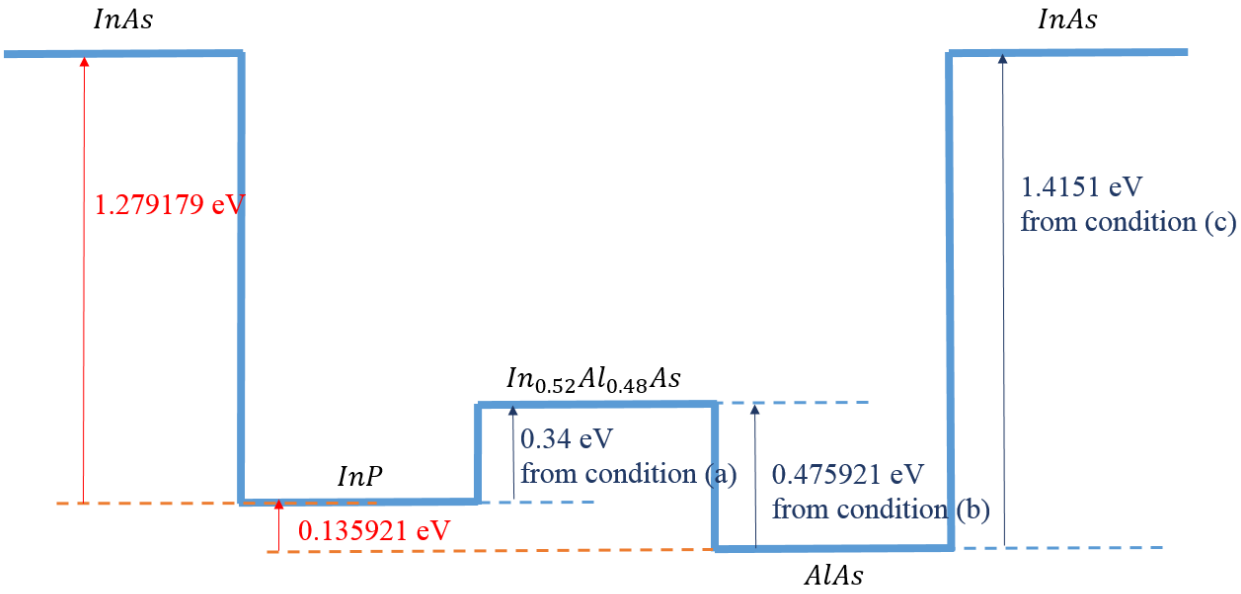

Figure12.Conduction band energy level relationships of the $In_{0.52}Al_{0.48}As$/InAs/AlAs/ InP family.

As Shown in Figure 12, we can calculate the conduction band discontinuity of InP to AlAs by substrate 0.475921 eV to 0.34 eV, so 0.135921 is obtained.

For the the conduction band discontinuity of InAs to InP: $1.4151\ \text{eV} - 0.135921\ \text{eV} = 1.279179\ \text{eV}$, which is the largest quantum well potential that we are able to design in InAlAs/InP design when using InP as the material of the single well.

For calculating the $In_{1-x}Al_xAs$/InP conduction band discontinuity, the relationship of them is plotted as Figure 13.

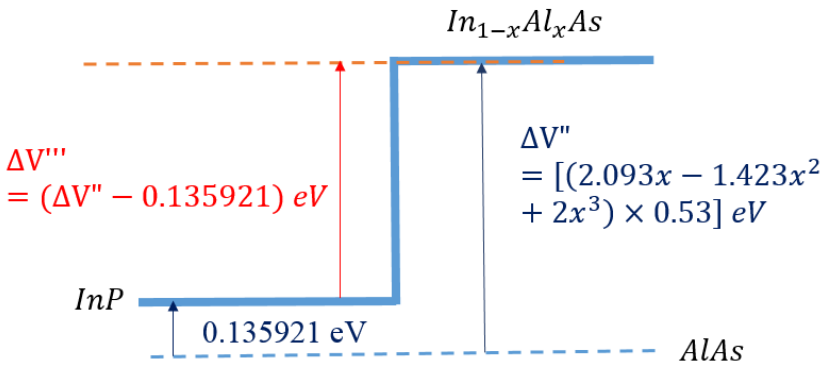

Figure 13. Conduction band discontinuity of $In_{1-x}Al_xAs/InP$.

According to Figure 13,

$$\Delta V''' = (\Delta V'' - 0.135921)\ eV$$
$$= [(2.093x - 1.423x^2 + 2x^3) \times 0.53 - 0.135921]\ \text{eV} \quad (2.29)$$

2.3.2 Structure designed for $In_{1-x}Al_xAs/InP$

Pluging all the parameters we got to calculate the single-double well design in $In_{1-x}Al_xAs/InP$ material.

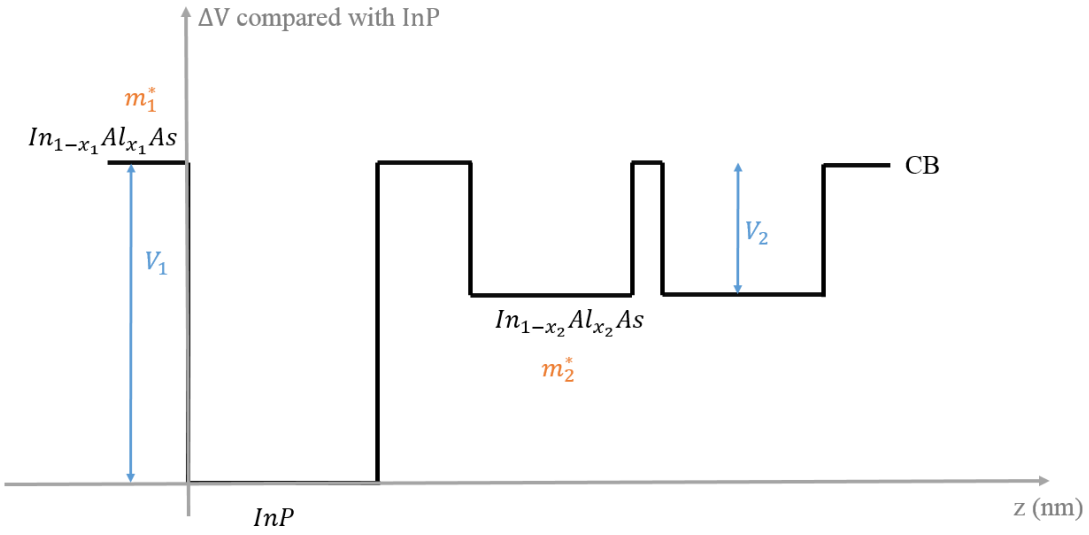

Figure 14. Single-Double Quantum Well Design in $In_{1-x}Al_xAs/InP$ material.

For the conduction band (CB) changes compared with InP conduction band is depicted in Figure 14 for the structure made consideration.

The value of V1 and V2 in Figure 14 are given in terms of:

$$V_1 = [(2.093x_1 - 1.423x_1^2 + 2x_1^3) \times 0.53 - 0.135921] \tag{2.30}$$

$$V_1 - V_2 = [(2.093x_2 - 1.423x_2^2 + 2x_2^3) \times 0.53 - 0.135921] \tag{2.31}$$

The corresponding electron effective masses are,

$$m_1^* = (0.0427 + 0.0685x_1)m_0 \tag{2.32}$$

$$m_2^* = (0.0427 + 0.0685x_1)m_0 \tag{2.33}$$

as well as $m^*_{InP} = 0.08m_0$.

2.3.3 Simulation of $In_{1-x}Al_xAs/InP$ design

The Schrödinger equations for each of the regions of the $In_{1-x}Al_xAs/InP$ structure depicted in Figure 14 are:

$$-\frac{\hbar^2}{2m_0(0.0427+0.0685x_1)}\frac{\partial^2}{\partial z^2}\varphi_1(z) + [(2.093x_1 - 1.423x_1^2 + 2x_1^3)\times 0.53 - 0.135921]\varphi_1(z) = E\varphi_1(z) \quad \text{when } z \le 0$$

$$-\frac{\hbar^2}{2\times 0.08m_0}\frac{\partial^2}{\partial z^2}\varphi_2(z) = E\varphi_2(z) \quad \text{when } 0 \le z \le z_1$$

$$-\frac{\hbar^2}{2m_0(0.0427+0.0685x_1)}\frac{\partial^2}{\partial z^2}\varphi_3(z) + [(2.093x_1 - 1.423x_1^2 + 2x_1^3)\times 0.53 - 0.135921]\varphi_3(z) = E\varphi_3(z) \quad \text{when } z_1 \le z \le z_2 \quad (2.34)$$

$$-\frac{\hbar^2}{2m_0(0.0427+0.0685x_2)}\frac{\partial^2}{\partial z^2}\varphi_4(z) + [(2.093x_2 - 1.423x_2^2 + 2x_2^3)\times 0.53 - 0.135921]\varphi_4(z) = E\varphi_4(z) \quad \text{when } z_2 \le z \le z_3$$

$$-\frac{\hbar^2}{2m_0(0.0427+0.0685x_1)}\frac{\partial^2}{\partial z^2}\varphi_5(z) + [(2.093x_1 - 1.423x_1^2 + 2x_1^3)\times 0.53 - 0.135921]\varphi_5(z) = E\varphi_5(z)$$

when $z_3 \leq z \leq z_4$

$$-\frac{\hbar^2}{2m_0(0.0427+0.0685x_2)}\frac{\partial^2}{\partial z^2}\varphi_6(z) + [(2.093x_2 - 1.423x_2^2 + 2x_2^3) \times 0.53 - 0.135921]\varphi_6(z) = E\varphi_6(z)$$

when $z_4 \leq z \leq z_5$

$$-\frac{\hbar^2}{2m_0(0.0427+0.0685x_1)}\frac{\partial^2}{\partial z^2}\varphi_7(z) + [(2.093x_1 - 1.423x_1^2 + 2x_1^3) \times 0.53 - 0.135921]\varphi_7(z) = E\varphi_7(z)$$

when $z_5 \leq z$

where $\hbar = 1.054571628 \times 10^{-34}$, and $m_0 = 9.10938215 \times 10^{-31}$.

Coding them into Matlab, are varying x_1, x_2, z_1, z_2, z_3, z_4, and z_5 to optimize the energy matching conditions in the single-double quantum wells design, results in the design shown in Figure 15.

In the $In_{1-x}Al_xAs/InP$ design, the larger the x is, the higher the conduction band level will be.

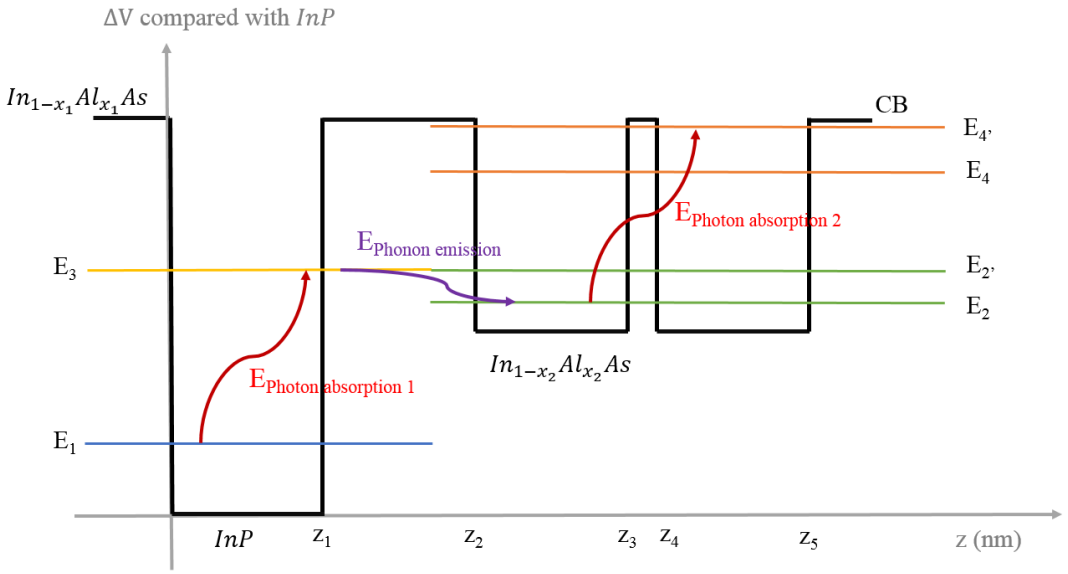

Figure 15. Simulation for single-double quantum well in $In_{1-x}Al_xAs$/InP material.

Figure 16 depicts the optimized structure for the design in $In_{1-x}Al_xAs$/InP material based on many calculations performed by adjusting these parameters.

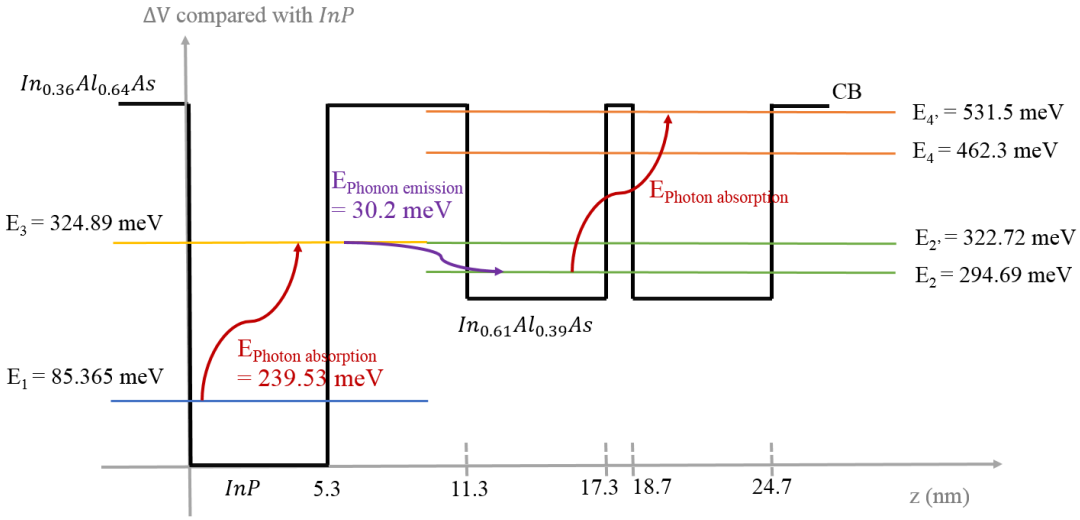

Figure 16. Result of signal-to-noise enhanced photodetector in $In_{1-x}Al_xAs$/InP material.

For the single well, $In_{0.36}Al_{0.64}As$ is used as barrier, and InP is used for the well. The potential of the single well then turns out to be 542.981 meV. For the double well, $In_{0.36}Al_{0.64}As$ is still the barrier, both outside the double well and between it, and now we use $In_{0.48}Al_{0.410}As$ as the well. A depth of 298.113 meV as potential of the double well is got.

In this result, we have the width of single well as 5.3 nm, and the width of each wells in double well as 6 nm. The barrier between the double well is 0.6 nm, and the barrier between single well and double well is 10 nm.

The energy states in single well then turn out to be E_1 = 85.365 meV, and E_3 = 32.489 meV. In the double well, energy states are E_2 = 294.69

meV, $E_{2'}$ = 322.72 meV, E_4 = 462.3 meV, and $E_{4'}$ = 531.5 meV as shown in Figure 16. The whole process for this signal-to-noise photodetector with material $In_{1-x}Al_xAs/InP$ material in this design works as follows:

i. From E_1 state, an electron absorbs one photon energy which equals to 239.53meV, having wavelength of 5176.80 nm, and jumps to E_3 state.

ii. The electron emits one phonon energy of 30.2 meV, with wavelength 41059.60 nm, and falls down to the state E_2.

iii. Absorbing another phonon with 236.81 meV (wavelength = 5236.27 nm) which having similar energy as the first one, the electron transitions to $E_{4'}$, which is very close to the barrier level of $In_{0.36}Al_{0.64}As$, and will be detected.

A range of light source which includes 5176.80 nm and 5236.27 nm will be detected by this apparatus.

2.4 Discussion

For the InGaAs design, the difference in the first and second absorbed photons is large. Since the light source for detecting needs to have a wide band at least from 6989.85 nm to 7269.74 nm, the wavelength difference is over 200 nm. A very wide band of source needed. Therefore, if we want to apply this InGaAs apparatus in practical use, it should be applied in the case of broad band light.

In the InAlAs/InP design, the barrier between single well and double

well is 10 nm, which is large for electron tunneling. The transmission coefficient for electrons tunneling in a rectangular barrier is:

$$\mathrm{T(E)} = \mathrm{e}^{-2\int_{x_1}^{x_2} dx\sqrt{\frac{2m}{\hbar^2}[V(x)-E]}} = \mathrm{e}^{-2(x_2-x_1)\sqrt{\frac{2m}{\hbar^2}(V_0-E)}} \tag{2.35}$$

Plugging in $\hbar = 1.054571628 \times 10^{-34}$, $\mathrm{m_0} = 9.10938215 \times 10^{-31}$, $x_2 - x_1 = 10 \times 10^{-9}\ (m)$, and $\mathrm{V_0} - E = 0.376\ \mathrm{(V)}$, the transmission coefficient $\mathrm{T} \approx 0$ is obtained.

The GaAlAs design thus seems to be the most promising in this Chapter, but we still want to work on reducing the barrier between single and double well to be less than 3 nm.

CHAPTER 3

INTERFACE PHONON MODES, DISPERSION CURVES, AND INTERFACE PHONON POTENTIAL CURVES IN SINGLE-DOUBLE QUANTUMWELL STRUCTURE

Herein, we are discussing the phonon modes in our single-double quantum well design. We also provide plots of the phonon dispersion curves. Also, phonon potential curves along the z direction of our structure with different wave vectors will be simulated as well.

Also, we fits the phonon emission energy to be the same as one of the phonon modes in the single-double quantum well structure because such interface phonon modes are more likely to produce a rapid phonon-assisted transfer for electrons. Then the potential curve of that phonon is plotted and used for the transfer efficiency simulation. [4, 5, 6]

3.1 Phonon Modes

Here, we determine the interface phonon modes in our structure and determine if there is a fit for the phonon emission energy.

3.1.1 Set up Regions for Single-double Quantum Wells

To begin, we set up the regions for this structure as Figure 17.

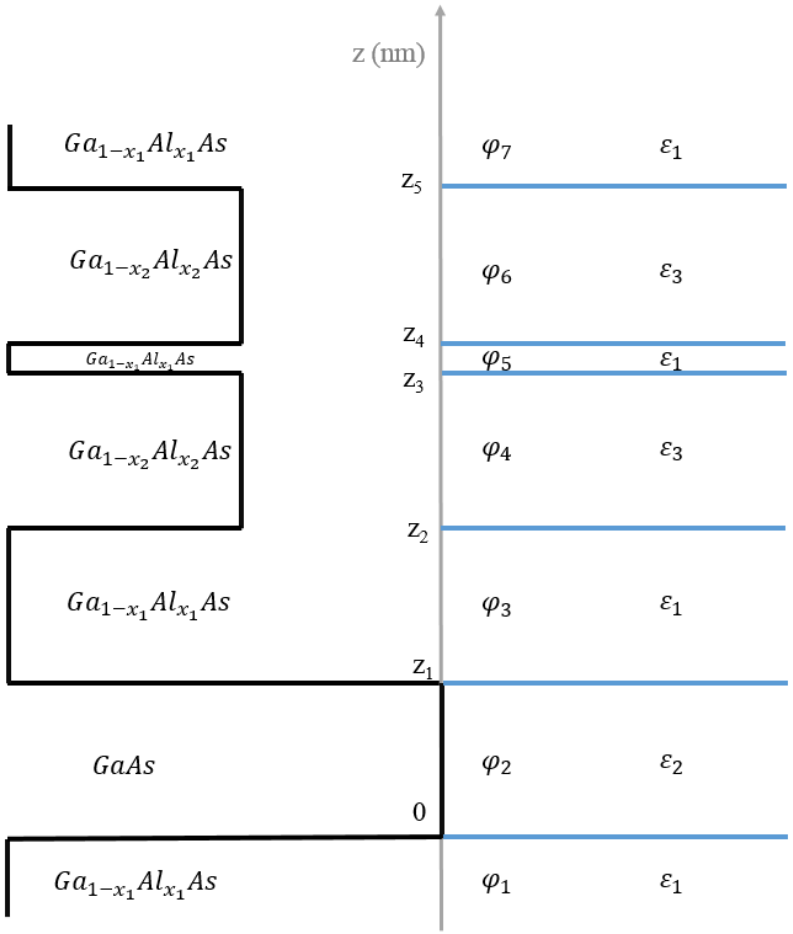

Figure 17. Sets the single-double quantum well structure into 7 regions.

Starting with the lowest layer, the phonon potential curves in each region is set to be φ_1, $\varphi_2, \varphi_3, \varphi_4$, φ_5, φ_6, and φ_7 respectively.

The dielectric function in $Ga_{1-x_1}Al_{x_1}As$ is set as ε_1; in $GaAs$ is set to be ε_2; and is set as ε_3 in $Ga_{1-x_2}Al_{x_2}As$.

For example, in the first region, where $z < 0$, the material we use is $Ga_{1-x_1}Al_{x_1}As$. The phonon potential is φ_1 along z direction, and the dielectric function is ε_1.

Example 2: in the fourth region, $z_2 \leq z < z_3$, the material used is $Ga_{1-x_2}Al_{x_2}As$. The phonon potential is φ_4 along z direction, and the dielectric function is ε_3.

3.1.2 Dielectric Function in GaAlAs System

For the binary heteromaterial GaAlAs, the dielectric function is:

$$\varepsilon(\omega) = \varepsilon^{\infty} \frac{(\omega_{LO-GaAs\ like}^2 - \omega^2)(\omega_{LO-AlAs\ like}^2 - \omega^2)}{(\omega_{TO-GaAs\ like}^2 - \omega^2)(\omega_{TO-AlAs\ like}^2 - \omega^2)} \tag{3.1}$$

and the dielectric function for materials like AlAs and GaAs,

$$\varepsilon(\omega) = \varepsilon^{\infty} \frac{(\omega_{LO}^2 - \omega^2)}{(\omega_{TO}^2 - \omega^2)} \tag{3.2}$$

The papermeters for ω_{LO}, ω_{TO} in GaAs and AlAs, and $\omega_{LO-GaAs\ like}$, $\omega_{TO-GaAs\ like}$, $\omega_{LO-AlAs\ like}$, and $\omega_{TO-AlAs\ like}$ are shown in Table I. [SeGi Yu, K.W. Kim, Michael A. Stroscio, G. J. Lafrate, J,-P. Sun et al, LAP, 82, 3363]

Table I. Dielectric parameters in GaAlAs/GaAs/AlAs material system.

	GaAs	**AlAs**	**$Ga_{1-x}Al_xAs$**
ε^{∞}	10.89	8.16	$10.89 - 2.73x$
$\hbar\omega_{LO-GaAs\ like}$ (meV)	36.25	---	$36.25 - 6.55x + 1.79x^2$
$\hbar\omega_{TO-GaAs\ like}$ (meV)	33.29	---	$33.29 - 0.64x - 1.16x^2$
$\hbar\omega_{LO-AlAs\ like}$ (meV)	---	50.09	$44.63 + 8.78x - 3.32x^2$
$\hbar\omega_{TO-AlAs\ like}$ (meV)	---	44.88	$44.63 + 0.55x - 0.30x^2$

In the design shown in Figure 17,

$$\varepsilon_1(\omega) = (10.89 - 2.73x_1) \times \frac{\left[(36.25 - 6.55x_1 + 1.79x_1^2)^2 - \omega^2\right]\left[(44.63 + 8.78x_1 - 3.32x_1^2)^2 - \omega^2\right]}{\left[(33.29 - 0.64x_1 - 1.16x_1^2)^2 - \omega^2\right]\left[(44.63 + 0.55x_1 - 0.30x_1^2)^2 - \omega^2\right]} \tag{3.3}$$

$$\varepsilon_2(\omega) = 10.89\frac{(36.25^2 - \omega^2)}{(33.29^2 - \omega^2)} \tag{3.4}$$

$$\varepsilon_3(\omega) = (10.89 - 2.73x_2) \times \frac{\left[(36.25 - 6.55x_2 + 1.79x_2^2)^2 - \omega^2\right]\left[(44.63 + 8.78x_2 - 3.32x_1^2)^2 - \omega^2\right]}{\left[(33.29 - 0.64x_2 - 1.16x_2^2)^2 - \omega^2\right]\left[(44.63 + 0.55x_2 - 0.30x_2^2)^2 - \omega^2\right]} \tag{3.5}$$

3.1.3 Solve Boundary Conditions

Before solving the boundary conditions, interface phonon potential curves for seven regions as shown in Figure 17 are needed using the general expressions,

$$\varphi_1 = Ae^{qz} \quad \text{when } z \leq 0$$

$$\varphi_2 = Be^{qz} + Ce^{-qz} \quad \text{when } 0 \leq z \leq z_1 \tag{3.6}$$

$$\varphi_3 = De^{q(z-z_1)} + Ee^{-q(z-z_1)} \quad \text{when } z_1 \leq z \leq z_2$$

$$\varphi_4 = \mathrm{F}e^{q(z-z_2)} + \mathrm{G}e^{-q(z-z_2)}$$

when $z_2 \leq z \leq z_3$

$$\varphi_5 = \mathrm{H}e^{q(z-z_3)} + \mathrm{I}e^{-q(z-z_3)}$$

when $z_3 \leq z \leq z_4$

$$\varphi_6 = \mathrm{J}e^{q(z-z_4)} + \mathrm{K}e^{-q(z-z_4)}$$

when $z_4 \leq z \leq z_5$

$$\varphi_7 = \mathrm{L}e^{-q(z-z_5)}$$

when $z_5 \leq z$

where q is the wave vector, we can use the following boundary conditions:

$$\varphi_n(z) = \varphi_{n+1}(z) \tag{3.7}$$

$$\varepsilon_n \frac{\partial \varphi_n(z)}{\partial z} = \varepsilon_{n+1} \frac{\partial \varphi_{n+1}(z)}{\partial z} \tag{3.8}$$

to obtain relations among these constants.

i. Solving the boundary conditions at $z = 0$, from equation (3.7):

$$\varphi_1(0) = \varphi_2(0) \tag{3.9}$$

$$\mathrm{A}e^{q\times 0} = \mathrm{B}e^{q\times 0} + \mathrm{C}e^{-q\times 0} \tag{3.10}$$

$$\mathrm{A} = \mathrm{B} + \mathrm{C} \tag{3.11}$$

From the second boundary condition (3.8), taking $z = 0$ in:

$$\varepsilon_1 \frac{\partial \varphi_1(0)}{\partial z} = \varepsilon_2 \frac{\partial \varphi_2(0)}{\partial z} \tag{3.12}$$

$$\varepsilon_1 \times \mathrm{qAe}^{\mathrm{q}\times 0} = \varepsilon_2 \times \mathrm{qBe}^{\mathrm{q}\times 0} + \varepsilon_2 \times (-\mathrm{q})\mathrm{Ce}^{-\mathrm{q}\times 0} \tag{3.13}$$

We find,

$$\frac{\varepsilon_1}{\varepsilon_2}\mathrm{A} = \mathrm{B} - \mathrm{C}. \tag{3.14}$$

By solving equations (3.11) and (3.14), we can obtain:

$$\mathrm{B} = \frac{\mathrm{A}}{2}(1 + \frac{\varepsilon_1}{\varepsilon_2}) \tag{3.15}$$

$$\mathrm{C} = \frac{\mathrm{A}}{2}(1 - \frac{\varepsilon_1}{\varepsilon_2}) \tag{3.16}$$

ii. The boundary condition at $\mathrm{z} = \mathrm{z}_1$, for the first boundary condition (3.7),

$$\varphi_2(z_1) = \varphi_3(z_1), \tag{3.17}$$

yield,

$$\mathrm{Be}^{\mathrm{qz}_1} + \mathrm{Ce}^{-\mathrm{qz}_1} = \mathrm{De}^{\mathrm{q}\times 0} + \mathrm{Ee}^{-\mathrm{q}\times 0} \tag{3.18}$$

$$\mathrm{Be}^{\mathrm{qz}_1} + \mathrm{Ce}^{-\mathrm{qz}_1} = \mathrm{D} + \mathrm{E}. \tag{3.19}$$

From the second boundary condition (3.8),

$$\varepsilon_2 \frac{\partial \varphi_2(z_1)}{\partial z} = \varepsilon_1 \frac{\partial \varphi_3(z_1)}{\partial z}, \tag{3.20}$$

We obtain,

$$\varepsilon_2 \times \mathrm{qBe}^{\mathrm{qz}_1} + \varepsilon_2 \times (-\mathrm{q})\mathrm{Ce}^{-\mathrm{qz}_1} = \varepsilon_1 \times \mathrm{qDe}^{\mathrm{q}\times 0} + \varepsilon_1 \times (-\mathrm{q})\mathrm{Ee}^{-\mathrm{q}\times 0} \tag{3.21}$$

$$\frac{\varepsilon_2}{\varepsilon_1}(\mathrm{Be}^{\mathrm{qz}_1} - \mathrm{Ce}^{-\mathrm{qz}_1}) = \mathrm{D} - \mathrm{E}. \tag{3.22}$$

From (3.19) and (3.22),

$$\mathrm{D} = \frac{1}{2}\left[\left(1 + \frac{\varepsilon_2}{\varepsilon_1}\right)\mathrm{B}e^{qz_1} + \left(1 - \frac{\varepsilon_2}{\varepsilon_1}\right)\mathrm{C}e^{-qz_1}\right] \tag{3.23}$$

$$\mathrm{E} = \frac{1}{2}\left[\left(1 - \frac{\varepsilon_2}{\varepsilon_1}\right)\mathrm{B}e^{qz_1} + \left(1 + \frac{\varepsilon_2}{\varepsilon_1}\right)\mathrm{C}e^{-qz_1}\right] \tag{3.24}$$

iii. At $\mathrm{z} = \mathrm{z}_2$, for the first boundary condition (3.7),

$$\varphi_3(z_2) = \varphi_4(z_2), \tag{3.25}$$

yield,

$$\mathrm{D}e^{q(z_2 - z_1)} + \mathrm{E}e^{-q\times(z_2 - z_1)} = \mathrm{F}e^{q\times 0} + \mathrm{G}e^{-q\times 0} \tag{3.26}$$

$$\mathrm{D}e^{q(z_2 - z_1)} + \mathrm{E}e^{-q\times(z_2 - z_1)} = \mathrm{F} + \mathrm{G}. \tag{3.27}$$

From the second boundary condition (3.8),

$$\varepsilon_1 \frac{\partial\varphi_3(z_2)}{\partial z} = \varepsilon_3 \frac{\partial\varphi_4(z_2)}{\partial z}, \tag{3.28}$$

We obtained,

$$\begin{aligned}\varepsilon_1 \times q\mathrm{D}e^{q(z_2 - z_1)} + \varepsilon_1 \times (-q)\mathrm{E}e^{-q(z_2 - z_1)} \\ = \varepsilon_3 \times q\mathrm{F}e^{q\times 0} + \varepsilon_3 \times (-q)\mathrm{G}e^{-q\times 0}\end{aligned} \tag{3.29}$$

$$\frac{\varepsilon_1}{\varepsilon_3}(\mathrm{D}e^{q(z_2 - z_1)} - \mathrm{E}e^{-q(z_2 - z_1)}) = \mathrm{F} - \mathrm{G}. \tag{3.30}$$

From (3.27) and (3.30), we find,

$$\mathrm{F} = \frac{1}{2}\left[\left(1 + \frac{\varepsilon_1}{\varepsilon_3}\right)\mathrm{D}e^{q(z_2 - z_1)} + \left(1 - \frac{\varepsilon_1}{\varepsilon_3}\right)\mathrm{E}e^{-q(z_2 - z_1)}\right] \tag{3.31}$$

$$G = \frac{1}{2}\left[\left(1 - \frac{\varepsilon_1}{\varepsilon_3}\right) De^{q(z_2 - z_1)} + \left(1 + \frac{\varepsilon_1}{\varepsilon_3}\right) Ee^{-q(z_2 - z_1)}\right]. \tag{3.32}$$

iv. At $z = z_3$, for the first boundary condition (3.7), yields,

$$Fe^{q(z_3 - z_2)} + Ge^{-q(z_3 - z_2)} = H + I. \tag{3.33}$$

From the second boundary condition (3.8), we have,

$$\frac{\varepsilon_3}{\varepsilon_1}(Fe^{q(z_3 - z_2)} - Ge^{-q(z_3 - z_2)}) = H - I. \tag{3.34}$$

From (3.33) and (3.34), we find,

$$H = \frac{1}{2}\left[\left(1 + \frac{\varepsilon_3}{\varepsilon_1}\right) Fe^{q(z_3 - z_2)} + \left(1 - \frac{\varepsilon_3}{\varepsilon_1}\right) Ge^{-q(z_3 - z_2)}\right] \tag{3.35}$$

$$I = \frac{1}{2}\left[\left(1 - \frac{\varepsilon_3}{\varepsilon_1}\right) Fe^{q(z_3 - z_2)} + \left(1 + \frac{\varepsilon_3}{\varepsilon_1}\right) Ge^{-q(z_3 - z_2)}\right]. \tag{3.36}$$

v. At $z = z_4$, the fifth interface, for the first boundary condition (3.7),

$$He^{q(z_4 - z_3)} + Ie^{-q(z_4 - z_3)} = J + K. \tag{3.37}$$

From the second boundary condition (3.8),

$$\frac{\varepsilon_1}{\varepsilon_3}\left(He^{q(z_4 - z_3)} - Ie^{-q(z_4 - z_3)}\right) = J - K. \tag{3.38}$$

From (3.37) and (3.38), we find,

$$J = \frac{1}{2}\left[\left(1 + \frac{\varepsilon_1}{\varepsilon_3}\right) He^{q(z_4 - z_3)} + \left(1 - \frac{\varepsilon_1}{\varepsilon_3}\right) Ie^{-q(z_4 - z_3)}\right] \tag{3.39}$$

$$K = \frac{1}{2}\left[\left(1 - \frac{\varepsilon_1}{\varepsilon_3}\right) He^{q(z_4 - z_3)} + \left(1 + \frac{\varepsilon_1}{\varepsilon_3}\right) Ie^{-q(z_4 - z_3)}\right]. \tag{3.40}$$

vi. At the final interface $z = z_5$, from the first boundary condition (3.7), we

find,

$$\mathrm{J}e^{q(z_5-z_4)} + \mathrm{K}e^{-q(z_5-z_4)} = \mathrm{L}, \tag{3.41}$$

and from the second boundary condition (3.8), we find,

$$-\frac{\varepsilon_3}{\varepsilon_1}\left(\mathrm{J}e^{q(z_5-z_4)} - \mathrm{K}e^{-q(z_5-z_4)}\right) = \mathrm{L}. \tag{3.42}$$

From (3.41) and (3.42), we have,

$$\frac{\mathrm{J}e^{q(z_5-z_4)}+\mathrm{K}e^{-q(z_5-z_4)}}{\mathrm{J}e^{q(z_5-z_4)}-\mathrm{K}e^{-q(z_5-z_4)}} = -\frac{\varepsilon_3}{\varepsilon_1}, \tag{3.43}$$

and this equation can be used for solving interface phonon modes. All the ω consent (3.40) are the interface phonon modes in this structure.

From the above, all hetero-interface are solved. All the constants, B, C, D, E, F, G, H, I, J, K, and L, are able to be represented by constant A. From equations (3.12), (3.13), (3.20), (3.21), (3.28), (3.29), (3.32), (3.33), (3.36), (3.37), (3.39), their relationships can be summed up as follows:

$$\mathrm{B} = \frac{\mathrm{A}}{2}\left(1 + \frac{\varepsilon_1}{\varepsilon_2}\right)$$

$$\mathrm{C} = \frac{\mathrm{A}}{2}\left(1 - \frac{\varepsilon_1}{\varepsilon_2}\right)$$

$$\mathrm{D} = \frac{1}{2}\left[\left(1 + \frac{\varepsilon_2}{\varepsilon_1}\right)\mathrm{B}e^{qz_1} + \left(1 - \frac{\varepsilon_2}{\varepsilon_1}\right)\mathrm{C}e^{-qz_1}\right] \tag{3.44}$$

$$\mathrm{E} = \frac{1}{2}\left[\left(1 - \frac{\varepsilon_2}{\varepsilon_1}\right)\mathrm{B}e^{qz_1} + \left(1 + \frac{\varepsilon_2}{\varepsilon_1}\right)\mathrm{C}e^{-qz_1}\right]$$

$$\mathrm{F} = \frac{1}{2}\left[\left(1 + \frac{\varepsilon_1}{\varepsilon_3}\right)\mathrm{D}e^{q(z_2-z_1)} + \left(1 - \frac{\varepsilon_1}{\varepsilon_3}\right)\mathrm{E}e^{-q(z_2-z_1)}\right]$$

$$G = \frac{1}{2}\left[\left(1 - \frac{\varepsilon_1}{\varepsilon_3}\right) De^{q(z_2 - z_1)} + \left(1 + \frac{\varepsilon_1}{\varepsilon_3}\right) Ee^{-q(z_2 - z_1)}\right]$$

$$H = \frac{1}{2}\left[\left(1 + \frac{\varepsilon_3}{\varepsilon_1}\right) Fe^{q(z_3 - z_2)} + \left(1 - \frac{\varepsilon_3}{\varepsilon_1}\right) Ge^{-q(z_3 - z_2)}\right]$$

$$I = \frac{1}{2}\left[\left(1 - \frac{\varepsilon_3}{\varepsilon_1}\right) Fe^{q(z_3 - z_2)} + \left(1 + \frac{\varepsilon_3}{\varepsilon_1}\right) Ge^{-q(z_3 - z_2)}\right]$$

$$J = \frac{1}{2}\left[\left(1 + \frac{\varepsilon_1}{\varepsilon_3}\right) He^{q(z_4 - z_3)} + \left(1 - \frac{\varepsilon_1}{\varepsilon_3}\right) Ie^{-q(z_4 - z_3)}\right]$$

$$K = \frac{1}{2}\left[\left(1 - \frac{\varepsilon_1}{\varepsilon_3}\right) He^{q(z_4 - z_3)} + \left(1 + \frac{\varepsilon_1}{\varepsilon_3}\right) Ie^{-q(z_4 - z_3)}\right]$$

$$L = Je^{q(z_5 - z_4)} + Ke^{-q(z_5 - z_4)}$$

Now we substituting all the constants from B to L in the representations of A into (3.41); for example, $D = \frac{1}{2}\left[\left(1 + \frac{\varepsilon_2}{\varepsilon_1}\right)\frac{A}{2}\left(1 + \frac{\varepsilon_1}{\varepsilon_2}\right)e^{qz_1} + \left(1 - \frac{\varepsilon_2}{\varepsilon_1}\right)\frac{A}{2}(1 - \frac{\varepsilon_1}{\varepsilon_2})e^{-qz_1}\right]$. Also, with equations (3.3), (3.4), and (3.5), we can introduce ε_1, ε_2, and ε_3 in which depend on ω. An equation with ω to the power of 22 is obtained. Therefore, in this single-double quantum well structure based on GaAlAs/GaAs materials design, a total 22 interface phonon modes are found.

3.1.4 Phonon modes in GaAlAs design

We have written a Matlab codes (See Appendix B) for calculating the zero point solutions for:

$$f(\omega) = \frac{Je^{q(z_5 - z_4)} + Ke^{-q(z_5 - z_4)}}{Je^{q(z_5 - z_4)} - Ke^{-q(z_5 - z_4)}} + \frac{\varepsilon_3}{\varepsilon_1} \tag{3.45}$$

The solutions for (3.45) correspond to the phonon modes in the structure.

We now solve for the phonons in the GaAlAs design in Chapter 2 as Figure 8. In doing so, we use the parameters of Figure 18.

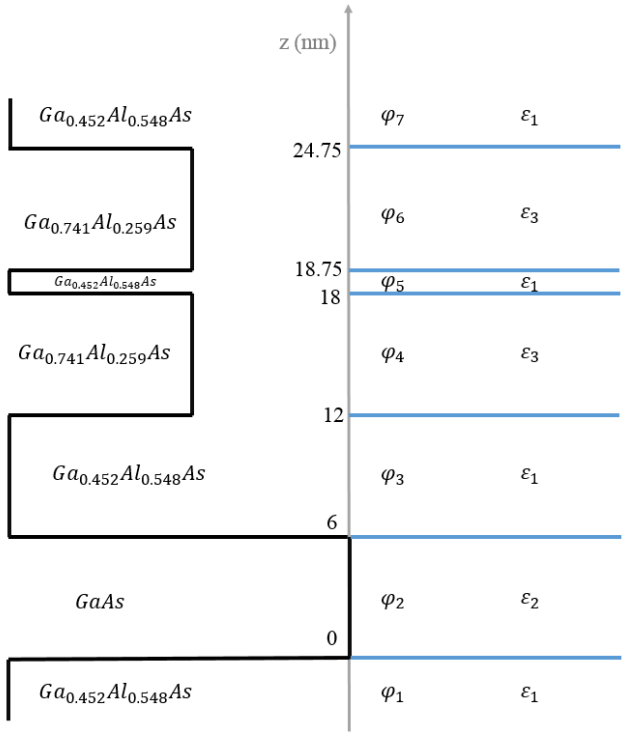

Figure18. Parameters in 7 regions for the $Ga_{0.452}Al_{0.548}As/GaAs/Ga_{0.741}Al_{0.259}As$ single-double quantum wells design as Figure 8 in Chapter 2.

For a wave vector with $q = 1 \times 10^8$ (m^{-1}), the 22 interface phonon modes are found to have the following energies:

32.59334 meV, 32.60926 meV, 32.65314 meV, 32.71726 meV, 32.85674 meV, 32.98312 meV, 33.2834 meV, 33.72162 meV, 34.17014 meV, 34.52196 meV, 34.82152 meV, 35.87928 meV, 44.75318 meV, 44.77414 meV, 44.80366 meV,

44.83792 meV, 45.63306 meV, 46.71746 meV, 47.19458 meV, 47.61638 meV, 48.10298 meV, and 48.41198 meV.

When the wave vector is $q = 2 \times 10^8$ (m^{-1}), the 22 interface phonon modes are found to have the following energies:

32.59842 meV, 32.63467 meV, 32.67191 meV, 32.69158 meV, 32.75729 meV, 32.91595 meV, 33.39435 meV, 34.00154 meV, 34.17864 meV, 34.65492 meV, 34.76901 meV, 35.48032 meV, 44.75497 meV, 44.77931 meV, 44.78831 meV, 44.83154 meV, 46.13702 meV, 46.78877 meV, 47.12994 meV, 47.55337 meV, 47.77569 meV, and 48.34654 meV.

Calculate phonon modes for different wave vectors from $q = 1 \times 10^8$ (m^{-1}) to $q = 5577446989 \cong 27.9 \times 10^8$ (m^{-1}), which equals to $\frac{\pi}{2a}$ where a is the lattice constant of GaAs 5.65325Å .

The interface phonon modes converge as the wave vector goes up, and when the wave vector $q = 15 \times 10^8$ (m^{-1}), there are only 4 remaining phonon modes: 32.68108 meV, 34.14631 meV, 44.78195 meV, and 47.58282 meV.

A plot of all the data on one graph, of phonon mode versus wave vector, represents the dispersion curve is as shown in Figure 19.

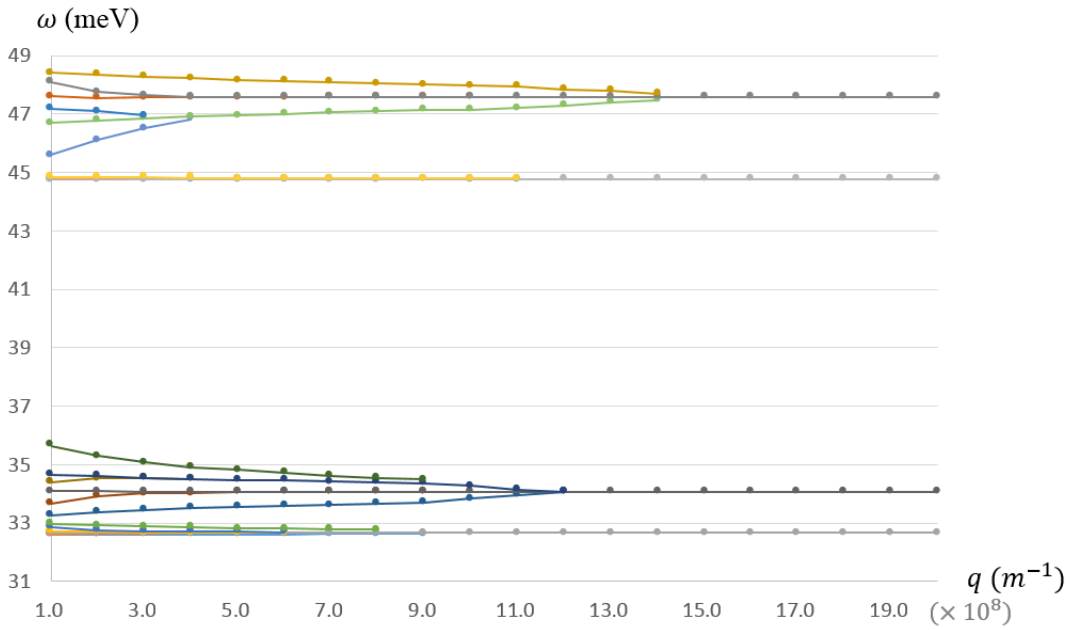

Figure 19. Dispersion curve of the $Ga_{0.452}Al_{0.548}As/GaAs/Ga_{0.741}Al_{0.259}$ single-double quantum wells design.

3.2 Phonon potential curves

For each phonon mode, there is one corresponding phonon potential curve along z direction of the structure. The phonon potential $\varphi(z)$ is what we discussed previously in Chapter 3.1.3 and listed in equation (3.6) as φ_1, φ_2, φ_3, φ_4 φ_5, φ_6, and φ_7 for each regions.

3.2.1 Constant A in $\varphi(z)$ Equations

Using the definition of normalization conditions as equation (3.46), we are able to solve constant A. This normalization condition is written as:

$$\frac{\hbar}{2\omega L^2} = \sum \frac{1}{4\pi}\frac{1}{2\omega}\frac{\partial \varepsilon_i(\omega)}{\partial \omega}\int dz(q^2|\varphi_i(q,z)|^2 + \left|\frac{\partial \varphi_i(q,z)}{\partial z}\right|^2) \tag{3.46}$$

We must evaluate $\int dz(q^2|\varphi_i(q,z)|^2 + \left|\frac{\partial \varphi_i(q,z)}{\partial z}\right|^2)$ for φ_1 to φ_7 in GaAlAs single-double quantum wells:

In the first region where $z \leq 0$, we have,

$$\int_{-\infty}^{0}(q^2|\varphi_1(q,z)|^2 + \left|\frac{\partial \varphi_1(q,z)}{\partial z}\right|^2)dz$$

$$= \int_{-\infty}^{0}[q^2|Ae^{qz}|^2 + (qAe^{qz})^2]dz \tag{3.47}$$

$$= \int_{-\infty}^{0} q^2A^2e^{2qz}dz = \frac{q^2}{2q}A^2e^{2qz}\Big|_{-\infty}^{0} = qA^2 - 0 = qA^2$$

For φ_2, we have,

$$\int_0^{z_1}(q^2|\varphi_2(q,z)|^2+\left|\frac{\partial\varphi_2(q,z)}{\partial z}\right|^2)dz$$

$$=\int_0^{z_1}[q^2|Be^{qz}+Ce^{-qz}|^2+(qBe^{qz}-qCe^{-qz})^2]dz$$

$$=\int_0^{z_1}[q^2(B^2e^{2qz}+2BCe^{qz}e^{-qz}+C^2e^{-2qz})$$

$$+q^2(B^2e^{2qz}-2BCe^{qz}e^{-qz}+C^2e^{-2qz})]dz \quad (3.48)$$

$$=\int_0^{z_1}2q^2(B^2e^{2qz}+C^2e^{-2qz})dz$$

$$=\frac{2q^2}{2q}(B^2e^{2qz}-C^2e^{-2qz})e^{2qz}\Big|_0^{z_1}$$

$$=q(B^2e^{2qz_1}-C^2e^{-2qz_1})-q(B^2-C^2)$$

$$=q[B^2(e^{2qz_1}-1)+C^2(1-e^{-2qz_1})]$$

For φ_3, φ_4 φ_5, φ_6, and φ_7, we find,

$$\int_{z_1}^{z_2}(q^2|\varphi_3(q,z)|^2+\left|\frac{\partial\varphi_3(q,z)}{\partial z}\right|^2)dz$$

$$=\frac{2q^2}{2q}(D^2e^{2q(z-z_1)}-E^2e^{-2q(z-z_1)})e^{2qz}\Big|_{z_1}^{z_2} \quad (3.48)$$

$$=q\left(D^2e^{2q(z_2-z_1)}-E^2e^{-2q(z_2-z_1)}\right)-q(D^2-E^2)$$

$$=q[D^2(e^{2q(z_2-z_1)}-1)+E^2(1-e^{-2q(z_2-z_1)})]$$

$$\int_{z_2}^{z_3}(q^2|\varphi_4(q,z)|^2+\left|\frac{\partial\varphi_4(q,z)}{\partial z}\right|^2)dz$$

$$=q[F^2(e^{2q(z_3-z_2)}-1)+G^2(1-e^{-2q(z_3-z_2)})]$$

$$\int_{z_3}^{z_4}(q^2|\varphi_5(q,z)|^2+\left|\frac{\partial\varphi_5(q,z)}{\partial z}\right|^2)dz$$

$$=q[H^2(e^{2q(z_4-z_3)}-1)+I^2(1-e^{-2q(z_4-z_3)})]$$

$$\int_{z_4}^{z_5}\left(q^2|\varphi_6(q,z)|^2+\left|\frac{\partial\varphi_6(q,z)}{\partial z}\right|^2\right)dz$$

$$=q[J^2(e^{2q(z_5-z_4)}-1)+K^2(1-e^{-2q(z_5-z_4)})]$$

$$\int_{z_5}^{\infty}(q^2|\varphi_7(q,z)|^2+\left|\frac{\partial\varphi_7(q,z)}{\partial z}\right|^2)dz$$

$$=\int_{z_5}^{\infty}\left[q^2\left|Le^{-q(z-z_5)}\right|^2+(qLe^{-q(z-z_5)})^2\right]dz$$

$$=\int_{z_5}^{\infty}q^2L^2e^{-2q(z-z_5)}dz=-\frac{q^2}{2q}L^2e^{-2q(z-z_5)}\Big|_{z_5}^{\infty}$$

$$=0-(-qL^2)=qL^2$$

With these results, equation (3.46) can be written in the form:

$$\frac{\partial \varepsilon_1(\omega)}{\partial \omega} qA^2 + \frac{\partial \varepsilon_2(\omega)}{\partial \omega} q[B^2(e^{2qz_1} - 1) + C^2(1 - e^{-2qz_1})]$$
$$+ \frac{\partial \varepsilon_1(\omega)}{\partial \omega} q\left[D^2\left(e^{2q(z_2 - z_1)} - 1\right) + E^2\left(1 - e^{-2q(z_2 - z_1)}\right)\right]$$
$$+ \frac{\partial \varepsilon_3(\omega)}{\partial \omega} q\left[F^2\left(e^{2q(z_3 - z_2)} - 1\right) + G^2\left(1 - e^{-2q(z_3 - z_2)}\right)\right]$$
$$+ \frac{\partial \varepsilon_1(\omega)}{\partial \omega} q\left[H^2\left(e^{2q(z_4 - z_3)} - 1\right) + I^2\left(1 - e^{-2q(z_4 - z_3)}\right)\right] \quad (3.49)$$
$$+ \frac{\partial \varepsilon_3(\omega)}{\partial \omega} q\left[J^2\left(e^{2q(z_5 - z_4)} - 1\right) + K^2\left(1 - e^{-2q(z_5 - z_4)}\right)\right]$$
$$+ \frac{\partial \varepsilon_1(\omega)}{\partial \omega} qL^2 = \frac{4\pi\hbar}{\boldsymbol{L^2}}$$

With all the constants from B to L being given in terms of A as shown previously, the equation that yields the value of A can now be solved. Matlab codes for solving of A are given in Appendix C.

Taking wave vector $q = 1 \times 10^8\ (m^{-1})$, we solved for all of the As for the interface phonon modes. The plots of the normalized potentials, φ(z), for each phonon are shown in Figure 20.

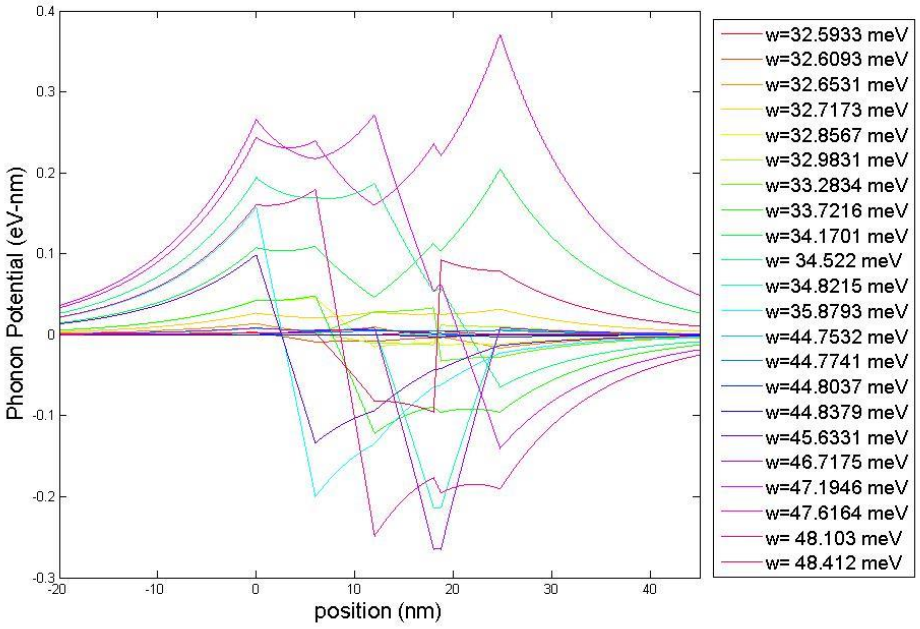

Figure 20. Interface phonon potential curves when $\mathbf{q} = \mathbf{1} \times \mathbf{10^8}\ (\boldsymbol{m^{-1}})$ in $Ga_{0.452}Al_{0.548}As/GaAs/Ga_{0.741}Al_{0.259}$ single-double quantum wells design.

For different wave vectors, the corresponding interface phonon potential curves may be plotted. In Figure 20, we plot graphs with some other wave vectors in the same structure.

Appendix D describes the Matlab codes for plotting interface phonon potential curves along the z direction of $Ga_{0.452}Al_{0.548}As/GaAs/Ga_{0.741}Al_{0.259}$ single-double quantum wells design.

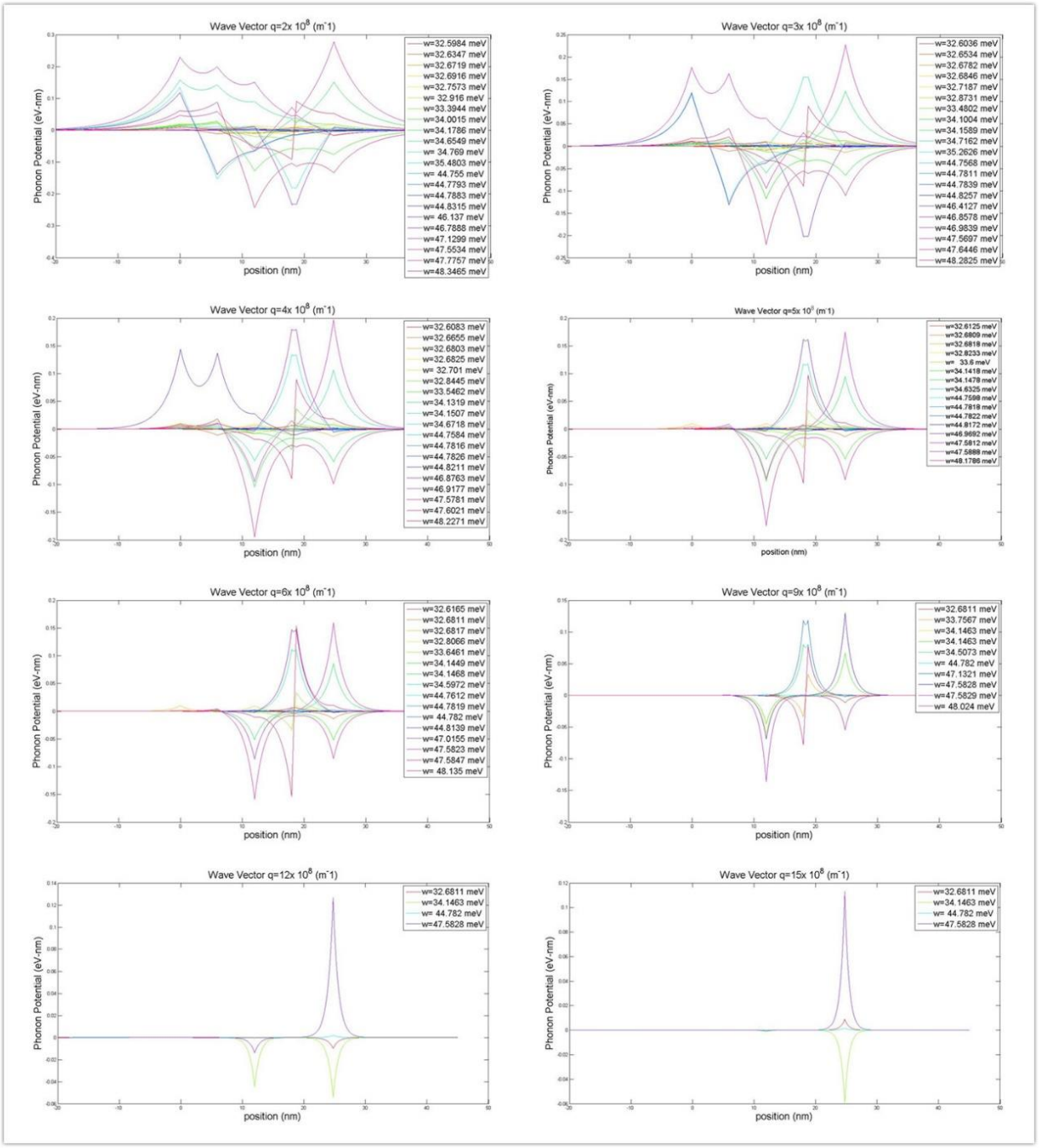

Figure 21. Interface phonon potential curves with different wave vectors in $Ga_{0.452}Al_{0.548}As/GaAs/Ga_{0.741}Al_{0.259}$ single-double quantum wells design.

CHAPTER 4

INTERFACE PHONON PROPERTIES IN ENHANCED SIGNAL-TO-NOISE PHOTODETECTOR WITH THE SINGLE WELL DELTA DOPED

In Chapter 1, we proposed the idea of the triple quantum well design with one single well and one double well. With this design, the photodetector absorbs one photon, emits a phonon, and absorbs another photon having the same energy as the first one. The signal-to-noise is enhanced as predicted by the Richardson formula since the total energy level changed of the electron is approximately twice that for the case of a photodetector based on one photon absorption. [7]

This series of processes – one photon absorption, one phonon emission, then one more photon absorption - works efficiently only if there is an excess electron kept in the first single well. In another words, electrons are needed to be enough for absorbing photons. [1, 4] Compared with uniform doping, a delta doping design is able to provide more electrons for absorption owing to the reduction of transition linewidth. [9, 10]

In this Chapter, phononic properties of single-double quantum wells with the single well delta doped will be described. [35]

---

[0]Parts of this thesis were reproduced with permission from © 2015 IEEE

4.1 Single-double Quantum Wells with Delta Doping

The design for a single-double quantum well photodetector with delta doping is shown in Figure 22.The wavefunction in Figure 22 were calculated by Chenjie using the self-consistent nextnano3 8-band k•p Schrödinger-Poisson solver [11]. An n-type doping of 6×10^{12} (cm^{-2}), where the volume density is

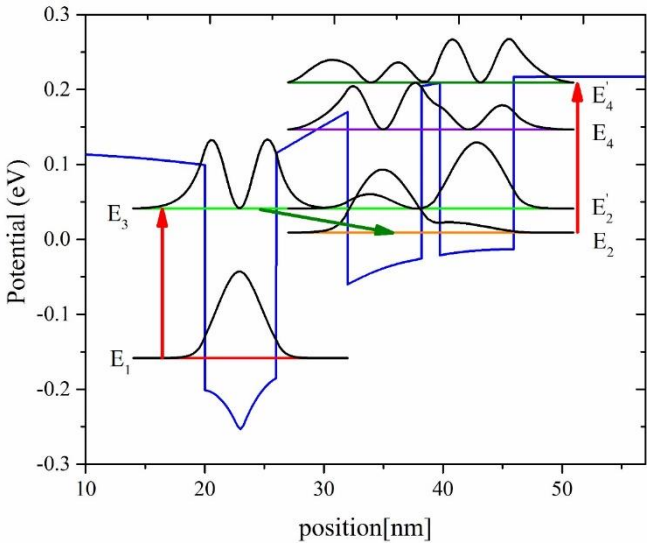

Figure 22. Signal-to-Noise enhanced photodetector with delta doping at the first well.

In this design, the photon absorption energy is 200 meV, and the phonon emission energy is 32.19 meV.

Other related information for this design follows:

i. $Al_{0.3594}Ga_{0.6406}As$ is used for the barriers.

ii. GaAs is used for the single well; $Al_{0.0841}Ga_{0.9159}As$ is used for the double

well.

iii. The barrier width between the single well and the double well is 6 nm, and the barrier width between the double well is 1.5383 nm.

iv. The width of the single well is 6 nm, and the width of each well in the double well is 6.2 nm.

4.2 Phonon Dispersion Curves for Delta Doping Design

4.2.1 Regions Defined the Interface Phonon Modes calculation

As known, the dielectric function for materials like AlAs and GaAs,

$$\varepsilon(\omega) = \varepsilon^{\infty} \frac{(\omega_{LO}^2 - \omega^2)}{(\omega_{TO}^2 - \omega^2)} \tag{4.1}$$

In which that the dielectric function for GaAs is altered negligibly by the concentration of n-type doping.

Since that in the single well region the dielectric function is kept the same, this single-double quantum well structure is still being defined in the 7 regions regardless to the n-type doping.

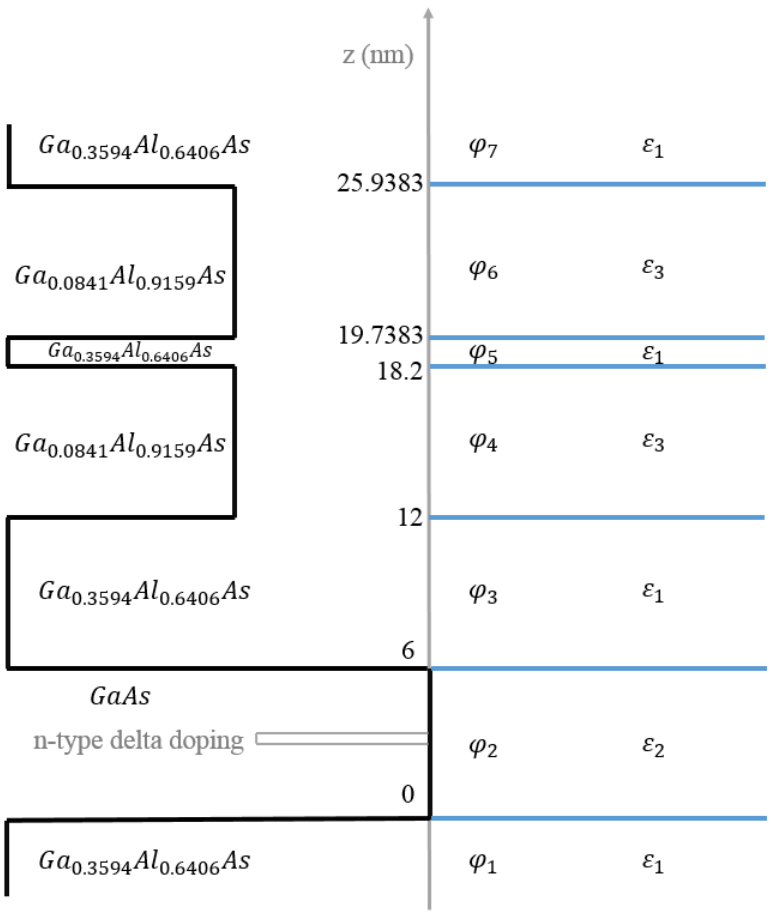

Figure 23. Parameter set for phononic properties simulation of delta-doping single-double quantum wells structure.

Phonon potential curves in each regions are set as follows:

$$\varphi_1 = \mathrm{A}e^{\mathrm{q}z} \quad \text{when } z \leq 0$$

$$\varphi_2 = \mathrm{B}e^{\mathrm{q}z} + \mathrm{C}e^{-\mathrm{q}z} \quad \text{when } 0 \leq z \leq 6 \tag{4.2}$$

$$\varphi_3 = \mathrm{D}e^{\mathrm{q}(z-6)} + \mathrm{E}e^{-\mathrm{q}(z-6)} \quad \text{when } 6 \leq z \leq 12$$

$$\varphi_4 = \mathrm{F}e^{q(z-12)} + \mathrm{G}e^{-q(z-12)}$$

when $12 \leq z \leq 18.2$

$$\varphi_5 = \mathrm{H}e^{q(z-18.2)} + \mathrm{I}e^{-q(z-18.2)}$$

when $18.2 \leq z \leq 19.7383$

$$\varphi_6 = \mathrm{J}e^{q(z-19.7383)} + \mathrm{K}e^{-q(z-19.7383)}$$

when $19.7383 \leq z \leq 25.9383$

$$\varphi_7 = \mathrm{L}e^{-q(z-25.9383)}$$

when $25.9383 \leq z$

where q is the wave vector, and A to L are the constants.

The dielectric functions for each regions are:

$$\varepsilon_1(\omega) = 9.141162 \times \frac{\left(32.72457^2 - \omega^2\right)\left(48.89208^2 - \omega^2\right)}{\left(32.40399^2 - \omega^2\right)\left(44.85922^2 - \omega^2\right)} \tag{4.3}$$

$$\varepsilon_2(\omega) = 10.89 \frac{(36.25^2 - \omega^2)}{(33.29^2 - \omega^2)} \tag{4.4}$$

$$\varepsilon_3(\omega) = 8.292405 \times \frac{\left(31.54311^2 - \omega^2\right)\left(49.9784^2 - \omega^2\right)}{\left(31.63083^2 - \omega^2\right)\left(44.88172^2 - \omega^2\right)} \tag{4.5}$$

4.2.2 Interface Phonon Dispersion Curves

Solving the boundary conditions [8] for 6 interfaces the result shown in Figure 23 are obtained

In obtaining these results, we used,

$$\varphi_n(z) = \varphi_{n+1}(z) \tag{3.7}$$

$$\varepsilon_n \frac{\partial \varphi_n(z)}{\partial z} = \varepsilon_{n+1} \frac{\partial \varphi_{n+1}(z)}{\partial z} \tag{3.8}$$

All of the interface phonon modes with different wave vectors can be plotted as the dispersion curves as Figure 24.

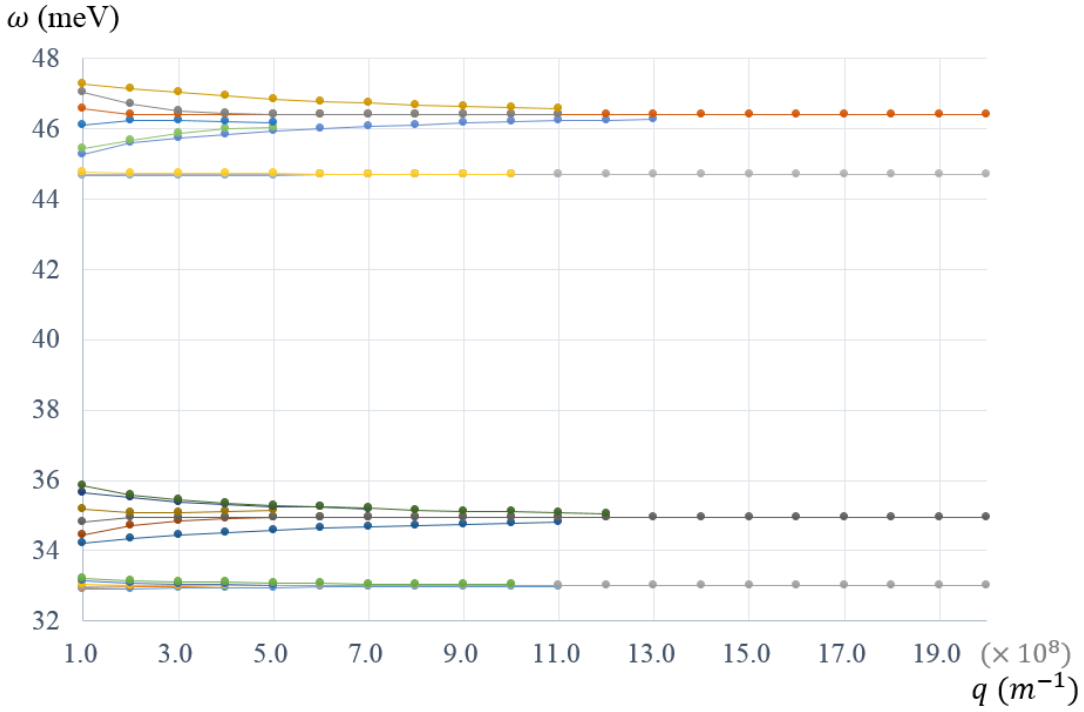

Figure 24. Dispersion curve of $Ga_{0.3594}Al_{0.6406}As/GaAs/Ga_{0.0841}Al_{0.9159}As$ structure with n-type doping in GaAs layer.

4.3 Interface Phonon Potential Curves for Delta Doping Design

Phonon modes with different wave vectors are calculated in section 4.2. In this section, simulation of the interface phonon potential curves along the z-direction of

the delta doping structure will be accomplished.

Using the normalization definition to solve for the constant A corresponding to each interface phonon modes, the curves for $\varphi(z)$ are obtained; these results are plotted as Figure 25.

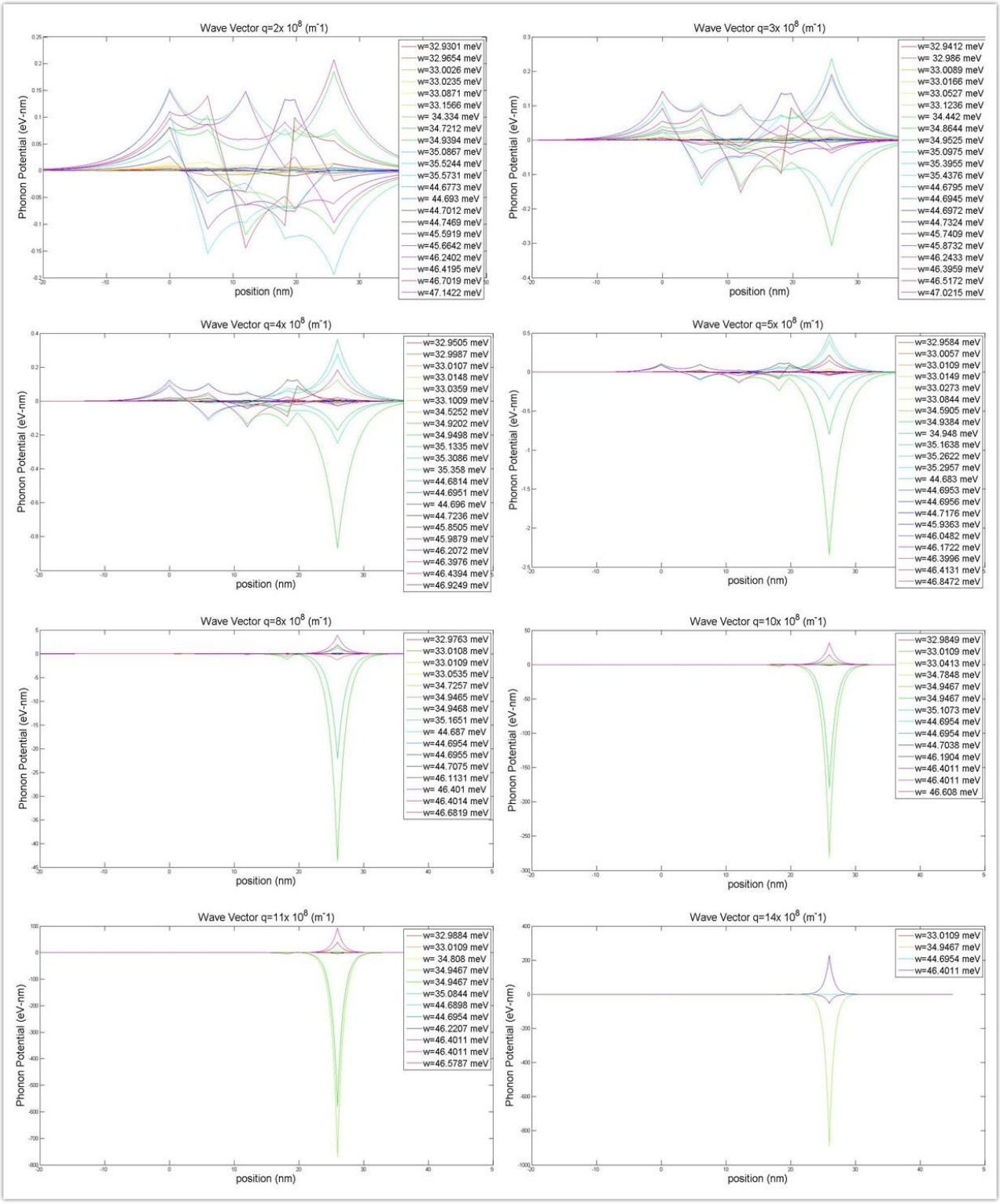

Figure 25. Interface phonon potential curves $\boldsymbol{\varphi}(\mathbf{z})$ for $Ga_{0.3594}Al_{0.6406}As/GaAs/Ga_{0.0841}Al_{0.9159}As$ structure with n-type doping in the GaAs layer.

CHAPTER 5

TRANSFER EFFICIENCY FOR THE SIGNAL-TO-NOISE ENHANCED PHOTODETECTOR

In the signal-to-noise enhanced photodetector mentioned in previous Chapters, there is a series relevant processes in the single-double well structure: a photon absorption, a phonon emission, and another photon absorption. In Chapter 4, delta-doping was added to provide enough electrons in the single well for appreciable photon absorption. In Chapter 5, another factor important in making the design effective – the phonon-assisted transition rate – is considered.

We would like the transmission time of the phonon to be very short, so that the electron will not accumulate in E_3 which might prevent the photon absorption from E_1 to E_3.

In this Chapter, the transfer efficiency in the GaAlAs design as Figure 8 will be calculated.

5.1 Fermi's Golden Rule

According to the Fermi's Golden Rule [1], we can consider the transfer efficiency,

$$\frac{1}{\tau_i} = \frac{2\pi}{\hbar}\sum_f \left|\langle f|\tilde{H}|i\rangle\right|^2 \delta(E_f - E_i) \tag{5.1}$$

where τ is the transfer efficiency, f is the final state wave function, i is the initial state wave function, and $\tilde{H}$ is the electron-phonon interaction, which is the charged times the phonon Frohlich potential.

We would like the overlap of the electronic wave functions and phonon potentials

to maximize the matrix element squared, in order to minimize the transition time so that it is short relative to the optical excitation rate.

5.2 Electronic Wave Functions

We use Matlab to perform the electronic wave function simulation. Codes are described in Appendix E.

Wave functions for the $Ga_{0.452}Al_{0.548}As/GaAs/Ga_{0.741}Al_{0.259}As$ system are then plotted as Figure 26.

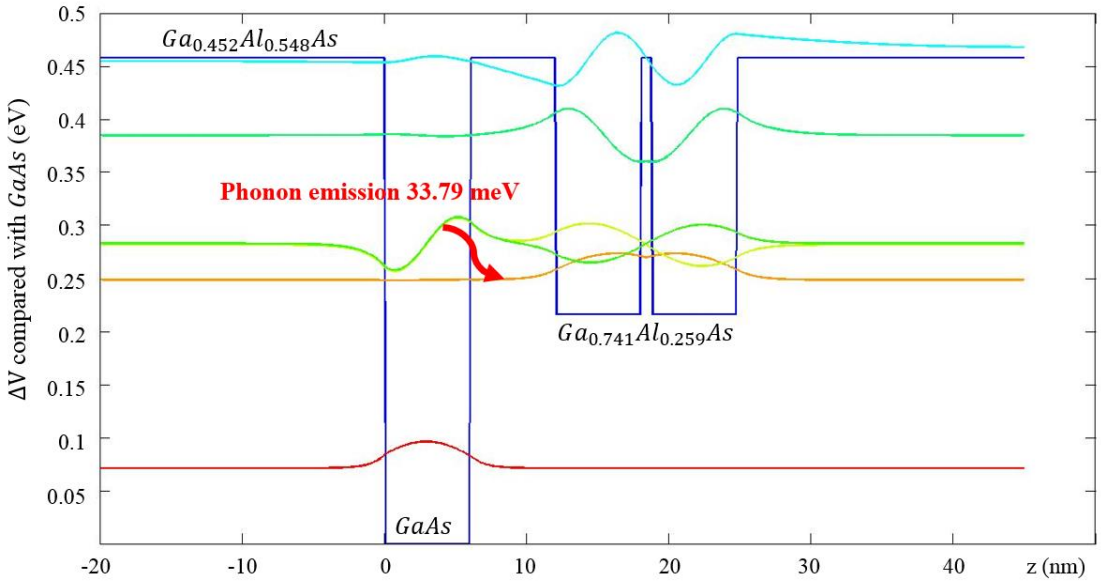

Figure 26. Wave functions for $Ga_{0.452}Al_{0.548}As/GaAs/Ga_{0.741}Al_{0.259}As$ single-double wells system.

After obtaining the wave functions, we are able to calculate the overlap area

squared $\left|\langle f|\tilde{H}|i\rangle\right|^2$ with the phonon potentials obtained in Chapter 3.

5.3 Simplified Structure

In reference [12], there is one simplified structure with GaAs/AlAs for which the calculated transfer time is $\frac{1}{6}$ ps for the phonon emission.

In this earlier calculation [12], the structure was a two well structure with GaAs as the material of barriers, and AlAs as the material of wells. The width of the first well was 8.5 nm, and the width of the second well was 18 nm. The barrier between two wells was 2 nm, and wave functions of the initial state and the final state for the phonon emission is shown as Figure 27.

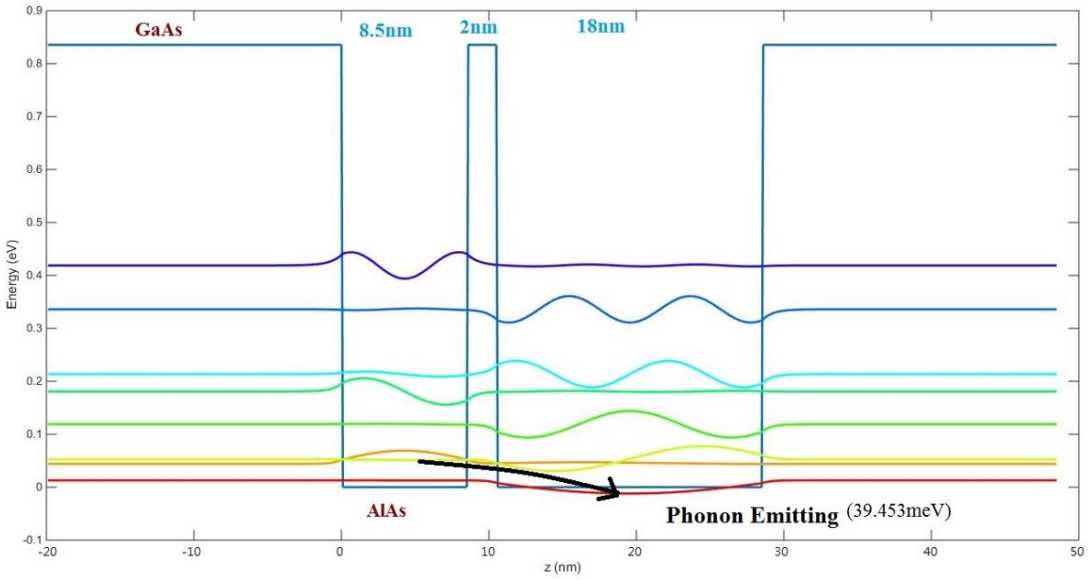

Figure 27. Wave functions for GaAs/AlAs two wells structure.

Be plotting out the phonon potential curves along the z direction the same way illustrated in Chapter 3, the matrix element squared $\left|\langle f|\tilde{H}|i\rangle\right|^2$, of this structure the overlaps in the matrix element can be visualized.

Moreover, direct overlap evaluation of the matrix element can be accomplished since we know all of the necessary function in the integrand.

The matrix element squared for Kisin's structure and $Ga_{0.452}Al_{0.548}As/GaAs/Ga_{0.741}Al_{0.259}As$ single-double quantum wells can now be made.

5.4 Overlap Area Squared Comparison

The matrix elements squared versus wave vector for the interface phonon modes is shown as Table II.

Table II. Comparison of matrix elements squared.

Wave Vector (q)	Squared	
	GaAs/AlAs Two Wells Structure	**$Ga_{0.452}Al_{0.548}As/GaAs/Ga_{0.741}Al_{0.259}As$ Single-double wells Structure**
$1 \times 10^8\ (m^{-1})$	0.711244	0.888536
$2 \times 10^8\ (m^{-1})$	0.340388	0.510229
$3 \times 10^8\ (m^{-1})$	0.163699	0.33412
$4 \times 10^8\ (m^{-1})$	0.055923	0.225603
$5 \times 10^8\ (m^{-1})$	0.00427	0.164965
$6 \times 10^8\ (m^{-1})$	0.014918	0.136989

$7 \times 10^8\ (m^{-1})$	0.013096	0.100969
$8 \times 10^8\ (m^{-1})$	0.010152	0.079547
$9 \times 10^8\ (m^{-1})$	0.008018	0.062362
$10 \times 10^8\ (m^{-1})$	0.006495	0.02879
$11 \times 10^8\ (m^{-1})$	0.00536	0.011562
$12 \times 10^8\ (m^{-1})$	0.004524	0.009932
$13 \times 10^8\ (m^{-1})$	0.003866	0.007885
$14 \times 10^8\ (m^{-1})$	0.003334	0.006387
$15 \times 10^8\ (m^{-1})$	0.002935	0.005677
Total	1.348223	2.573554

When the wave vector is larger than $15 \times 10^8\ (m^{-1})$, the overlap area is so small that can be neglected.

Since $\tau \propto \frac{1}{\left|\langle f|\widetilde{H}|i\rangle\right|^2}$, where $\left|\langle f|\widetilde{H}|i\rangle\right|^2$ is the square of overlap area. A phonon emission transferring time of 0.32 ps can be predicted in our structure. In another words, electrons leave E_3 with a life time of 0.32 ps.

CHAPTER 6

DNA-APTAMER-BASED SENSING OF IMMUNOGLOBULIN E WITH A GRAPHENE FIELD EFFECT-TRANSISTER-LIKE STRUCTURE

IgE, Immunoglobulin E, is an antibody associated with allergic reactions and immune-deficiency related diseases. In this work, we use DNA aptamers which are known to have the high selectivity to bind to the target molecules. In our case, we use a DNA aptamer that binds selectively to IgE.

In this research, a field-effect-transistor-like (FET-like) structure with a monolayer graphene between the source and drain is used. The IgE aptamer is bound to the graphene, and a voltage probe in an electrolyte is used for sensing the IgE target with the charge distribution.

6.1 Introduction

Aptamers are short DNA or RNA molecules and they are man-made through the technique of SELEX (Systematic Evolution of Ligands by Exponential enrichment). The SELEX method selects the highest affinity aptamer among a huge number of nucleotide sequences with the exposure of a target molecule. Because aptamers are small, they are an excellent alternative in high-selectivity applications to antibodies. [13, 16, 17, 20, 30] In our research, a 37-base DNA aptamer for IgE is used.

Graphene based FET-like substrates with DNA aptamer molecules as the sensing elements have been used for detection of ions and small molecules, such as K^+ and Pb^{2+} ions. [28, 29, 23, 25, 15] In previous research done by our group, the

graphene FET-like sensor was used to detect ions with the thrombin binding aptamer (TBA) functionalized on graphene layer. Methylene blue (MB), an electron donor, is bound to one end of the aptamer and a pyrene molecule is bound to the other terminus of the DNA aptamer. The pyrene is used to bind the aptamer to the graphene. When K+ and Pb2+ ions are introduced, they bind to the aptamer which brings the MB closer to the graphene and increases the current in the FET since that MB donates electrons. [30]

Herein, a liguid gate graphene-based FET with the Immunoglobulin E (IgE) aptamer attached on the monolayer of graphene is used to detect IgE protein. The IgE antibody plays an important role in allergic response and inflammation, so the detection of the IgE is useful in medical applications. [14] Comparing with the previous study mentioned above, the aptamer is not functionalized to MB anymore, but the detection is achieved by the changing in the charge distribution in the electrolyte. The binding of IgE and the IgE aptamer are shown in Figure 28.

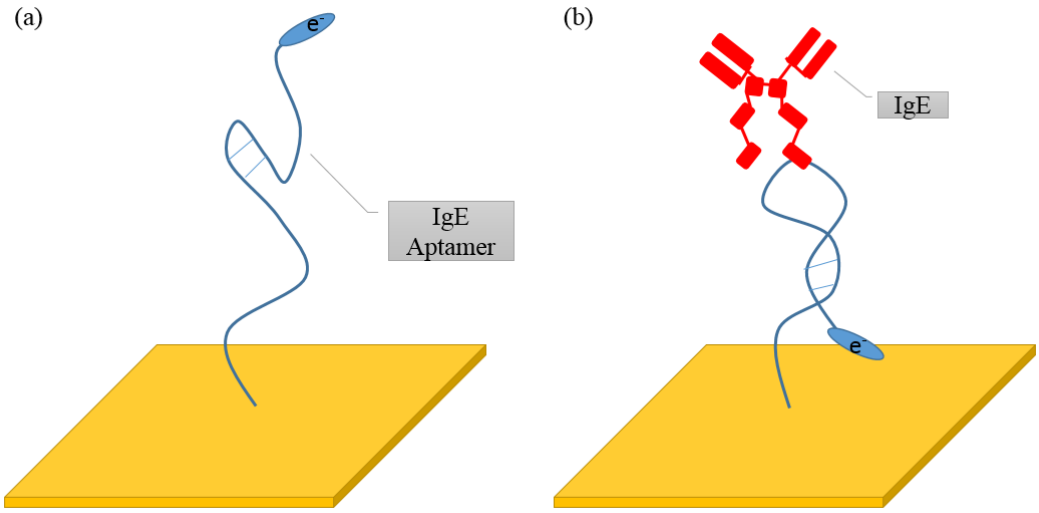

Figure 28. Charge distribution changed by the IgE and IgE aptamer interation.

The electrolyte used in this study is Phosphate buffered saline (PBS) which contains ions that screen charges introduced to the system. As shown in Figure 28, when the IgE target is added, the IgE aptamer bends and the charge goes near the praphene surface which will increase the conductivity of the graphene.

In this research, different concentrations of IgE targets are introduced to determine the sensing performance of this sensor.

6.2 Mono-layer Graphene FET structure

In the apparatus we are using, the graphene is attached on a biocompatible polydimethylsiloxane (PDMS) substrate, and source and drain of this FET-like structure are applied on the opposite ends of the graphene. Silver glue is pasted on the position of source and drain for conducting to the probe. For the gate, a well structure allowing liquid to be infused in is built on the graphene to form the liquid

gate.

The procedure of making this monolayer Graphene FET structure is as follows: [23]

i. Grow graphene on the Cu foil through CVD (chemical vapor deposition process. (Undergo some testing, such as Raman spectroscopy, SEM, and AFM, to check if there's only single layer of graphene on the Cu foil.)

ii. Attach PDMS on the graphene side of Cu foil.

iii. Etch away the cooper foil, and rinse with DI water (deionized water) several times.

iv. Deposit a frame like PDMS on the graphene to form a well.

v. Apply silver glue on the either hand sides of graphene out of the well.

The process above is described in Figure 29. In this research, these PDMS-graphene structures have been fabricated at the University of California at Irvine under the direction of Prof. Peter Burke. These structures are then transferred to UIC where tests over performed prior the use to ensure that the contacts function properly. Only then, is the graphene functionalize with the aptamer.

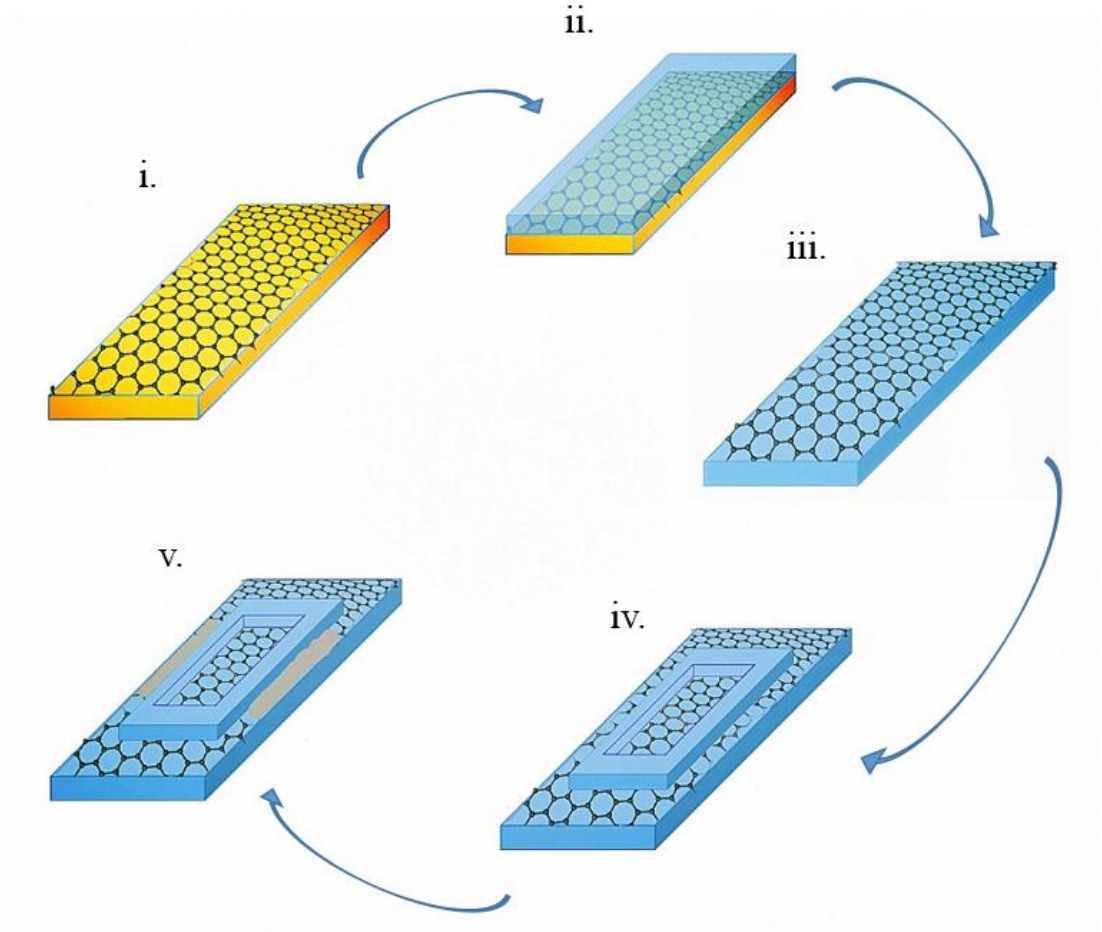

Figure 29. Procedure of mono-layer graphene FET fabrication.

6.3 Primary Test

In the primary test, also called the blank test, the quality of each FET sample is tested before the functionalization with IgE aptamers. Measurements of the I_{DS}-V_{DS} curve are made to ensure that it is if it's linear. Also, measurements of the I_{DS}-V_G curve ensure the completion of graphene. In a good FET device, the I_{DS}-V_G curve should perform in a V-shape as Figure 30.

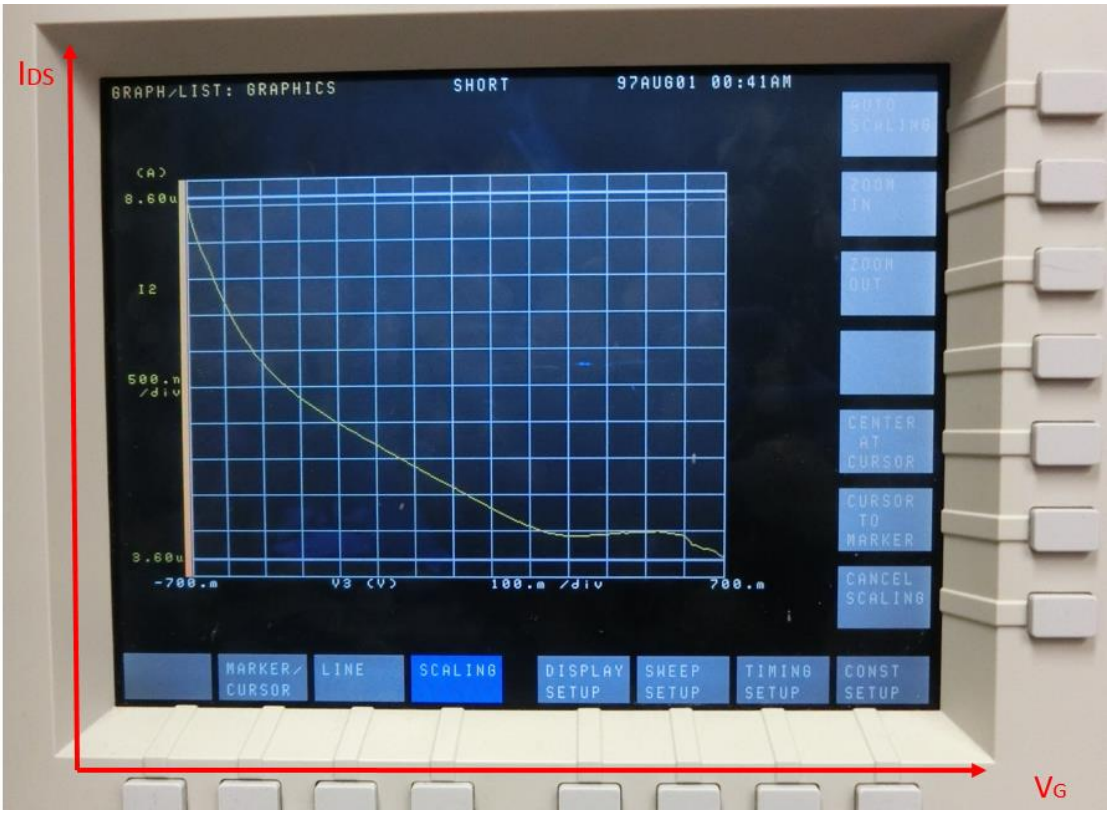

Figure 30. Blank test of I_{DS}-V_G curve for the monolayer graphene FET.

The full for the experiment circuit is connected as Figure 31. For testing the I_{DS}-V_G curve, V_{DS} is applied at a constant value. The voltage at V_G is varied to get the corresponding I_{DS} current value.

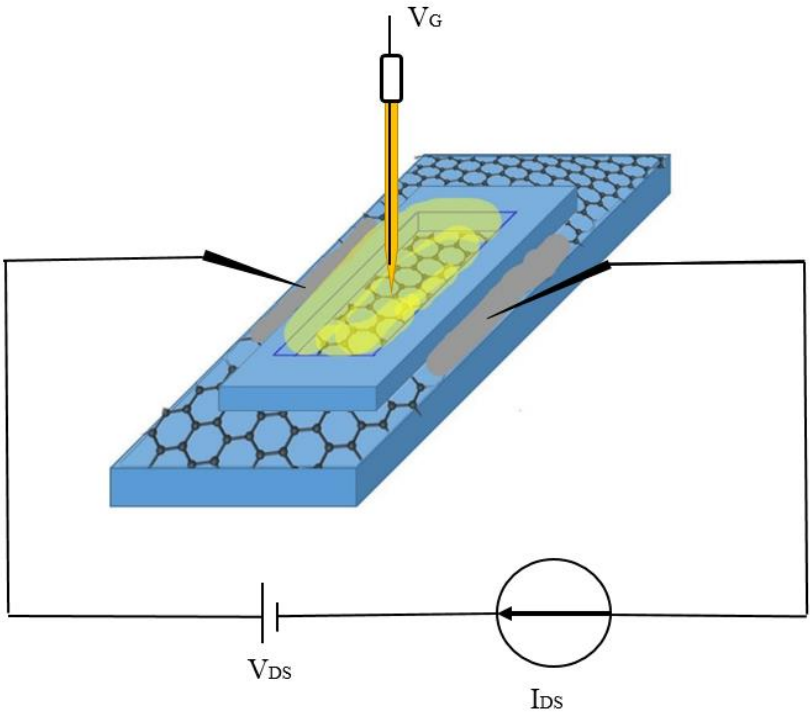

Figure 31. Circuit for the the monolayer graphene FET device.

6.4 IgE Aptamer and IgE Target

The selective IgE aptamers used in previous studies are listed as Table III.

Table III. IgE aptamers used in the corresponding references.

	IgE aptamer Sequence	Reference
(1)	5-NH2-GCG C GGGG CACG TTTA TCCG T CCC TCCTAGTGGCGTGCCCC GCGC-3	Khezrian, 2012 [18]
(2)	5'-NH2-GCG C GG GGC ACG TTT ATC CGT CCC TCC TAG TGG CGT GCC CCG CGC-3'	Maehashi, 2007 [19]
(3)	5'-NH2-GCG C GG GGC ACG TTT ATC CGT CCC TCC TAG TGG CGT GCC CCG CGC-3'	Ohno, 2010 [21]
(4)	5′-SH-GGG GCA CGT TTA TCC GTC CCT CCT AGT GGC GTG CCC C-3′	Wang, 2007 [22]

(5) 5’-SH-GGG GCA CGT TTA TCC GTC CCT CCT AGT GGC GTG CCC C-3’ Xu, 2005 [27]

Since the interaction between the aptamer and target must occurs within the Debye length [19], a shorter aptamer sequences are preferable. A 37-base aptamers present among all aptamers listed above is selected in this work:

5’-Pyrene-GGGG CACG TTTA TCCG T CCC TCCTAGTGGCGTGCCCC-3’

This aptamer is obtained from Biosearch Technologies (Novato, CA). The pyrene group next to the 5’ enables this IgE aptamer to bind to the graphene via π-π stacking.

The IgE target used in this study is obtained from Athens Research & Technology (Athens, GA).

6.5 Experiment

In this experiment, the IgE aptamer is bound to the graphene of the mono-layer graphene FET which will then sense the charges changing upon the interaction with IgE targets. When the charges near the graphene surface change as an result of the bending of IgE, the current through the source and drain should be increased as well.

6.5.1 Binding IgE Aptamers on Graphene

The process of binding the IgE aptamer to the graphene

i. 20 µL of 250 µM IgE aptamer in anhydrous Dimethylformamide (DMF) is dropped in the well of the FET device and left to incubate for three hours.

ii. Wash the well for three times with PBS (Phosphate-buffered saline), and

the well is then filled with 60 µL of PBS waiting for testing.

6.5.2 Gate Probe

For the gate probe, a flexible micro-reference Ag/AgCl electrode is connected. The Ag/AgCl electrode having 1mm tip was obtained from Microelectrodes, Inc. (Bedford, NH). Fill the glass filament with 3 M KCl solution and place it in the well for applying the gate voltage. The tip of the Ag/AgCl electrode should be placed in the middle of the solution, and not touching the bottom of the well to prevent damaging the graphene.

6.5.3 I_{DS}-V_G curves with Different Concentration of IgE

Steps for testing:

i. Test the I_{DS}-V_G curve with no IgE target but only 60 µL of PBS first

ii. Human Myeloma Plasma IgE is dissolved in DI H_2O to the concentration of 1 µM.

iii. 5 µL of 1 µM IgE solution is added in the well leaving for 2 minutes for the molecule to distribute uniformly. Test the I_{DS}-V_G curve again.

iv. Adding another 5 µL of 1 µM IgE solution, test another I_{DS}-V_G curve.

v. Several times of 5 µL of 1 µM IgE solution is needed to be added to test the I_{DS}-V_G performance for different concentrations.

Caution: During the experiment, the position of the probes for source, drain, and the gate has to be kept the same, or the primary standard resistance between source and drain, and from the graphene to the gate might be changed which might cause the experimental data to be unreliable. Therefore, for the whole apparatus the

circuit should be kept without any contact or even impact until all the I_{DS}-V_G curves are obtained with all the different concentrations of targets.

6.5.4 Controls

Two controls are done:

i. The IgE aptamer attached on the graphene-based FET device testing different concentrations of BSA (Bovine serum albumin) solution.

ii. No aptamer is attached on the graphene-based FET device testing different concentrations of IgE solution.

Also, in previous studies by Maehashi [19], the IgE aptamer was used on a CNT-FET sensor; herein, we use the same IgE aptamer. Because the CNT-FET sensor used in Maehashi's study was a p-type FET, IDS current decreased with higher concentrarion of IgE solution.

6.6 Results

6.6.1 IgE Aptamer Attached on Graphene-based FET Device Testing IgE Targets

In section 6.5.3, the one attached on the graphene is IgE aptamer, adding 5 µL of 1 µM IgE solution is added in turns into the well which already contains 60 µL of PBS. V_{DS} is applied at 300 mV.

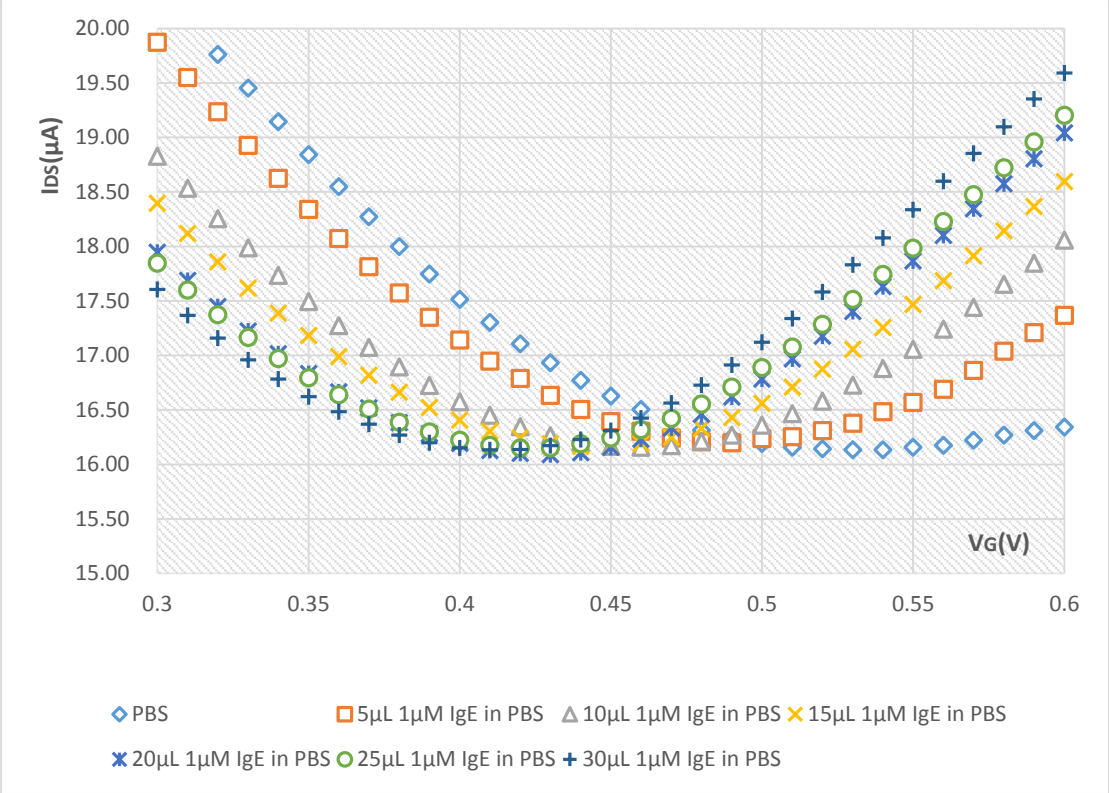

Figure 32. I_{DS}-V_G curve for IgE aptamer attached on graphene-based FET device testing IgE targets.

As shown in Figure 32, as the concentrations of IgE increased, I_{DS} current goes up in the n-conduction region, on the right side of the Dirac point, of graphene. On the opposite side, the I_{DS} current decreases in the p-conduction region when the concentrations of IgE is higher.

About the PBS, Phosphate-buffered saline, we added, it is a buffer solution used in biological research. It contains sodium dihydrogen phosphate, sodium chloride, etc.

Also, the Dirac points shifts left in voltage when the concentration of IgE is

higher. This shifting might be result from the n-type doping effect of the charge carriers.

The curve can be discussed in two parts: n-channel on the right side, and p-channel on the left side. In the n-channel, the major carrier is electrons; in the p-channel hold is the main carrier. Therefore, in the p-side, when the concentration of IgE increases, the amount of electrons to the surface of graphene is raised, the conductivity of the p-type conduction channel is reduced.

Table IV. Properties for IgE aptamer attached on graphene-based FET device testing IgE targets.

Volume of 1 μM IgE added (μL)	V_{Dirac} (V)	Minimum conduction current (μA)
0	0.54	16.133
5	0.49	16.200
10	0.46	16.158
15	0.45	16.164
20	0.43	16.090
25	0.42	16.153
30	0.41	16.134

6.6.2 IgE Aptamer Attached on Graphene-based FET Device Testing BSA Targets

As a control, BSA targets are added instead of IgE targets to the FET-device

still having IgE aptamer attached on the graphene. Applied V_{DS} is still 300 mV.

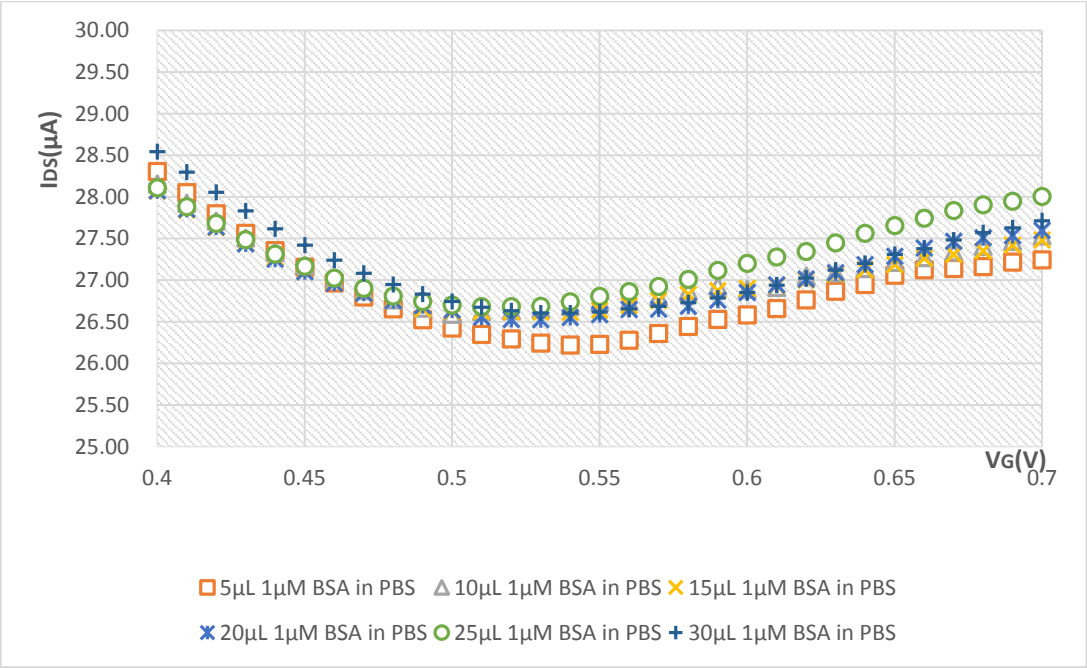

Figure 33. I_{DS}-V_G curve for IgE aptamer attached on graphene-based FET device testing BSA targets.

The result is predictable. Since the IgE aptamer should not be able to sense the BSA target, there should be no current changing which matches the result in Figure 33.

6.6.3 No Aptamer Attached on Graphene-based FET Device Testing IgE Targets

Another control is made by having no aptamer attached on the graphene, and the IgE target is still added in the well to see if there is any current changing.

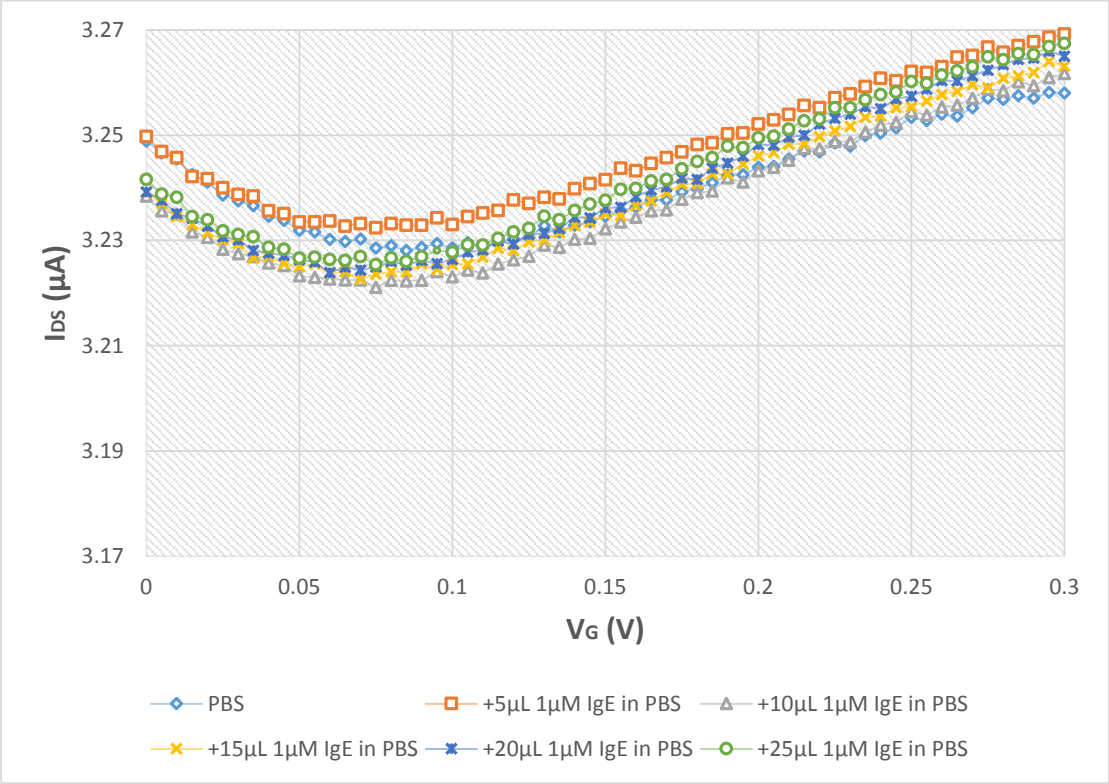

Figure 34. I_{DS}-V_G curve for no aptamer attached on graphene-based FET device testing IgE targets.

The result indicates that when no aptamer is attached on the graphene, the conductivity does not change with different concentrations of the target since there is no aptamer reacting with it.

6.7 Conclusion

The conductance of this graphene-FET sensor caused by the interaction of IgE target and the IgE aptamer is examined herein. As demonstrated herein, the IgE

molecule can be detected by this sensor, and also only a small voltage is needed for this apparatus, which makes it more applicable for small sensors in the future.

CITED LITERATURE

[1] Paul Harrison, Quantum Wells, Wires and Dot: Theoretical and Computational Physics, 3rd edition, (Wiley, New York, 2010).

[2] A. R. Bhatt, K. W. Kim, M. A. Stroscio, G. J. Iafrate, Mitra Dutta et al, Reduction of interface phonon modes using metalsemiconductor heterosturctures, Journal of Applied Physics 73, 2338 (1993).

[3] Hybertsen, Mark S.K., Band offset transitivity at the InGaAs/InAlAs/InP(001) heterointerfaces, Applied Physics Letters, Volume 58, Issue 16, April 22, 1991, pp.1759-1761.

[4] Michael A. Stroscio, Interface-Phonon--Assisted Transitions in Quantum Well Lasers, Journal of Applied Physics, 80, 6864 (1996); see also M. Stroscio and M. Dutta, Phonons in Nanostructures (Cambridge University Press. 2001).

[5] Mikhail V. Kisin, Vera B. Gorfinkel, Michael A. Stroscio, Gregory Belenky, and Serge Luryi, Influence of Complex Phonon Spectra on Intersubband Optical Gain, Journal of Applied Physics, 82, 2031 (1997).

[6] Michael A. Stroscio, Mihail Kisin, Gregory Belenke, and Serge Luryi, Phonon enhanced inverse population in asymmetric double quantum wells, Appl. Phys. Letts., 75, 3258-3260 (1999).

[7] Yi Lan, Nanzhu Zhang, J. L. Shi, M. Dutta, M. A. Stroscio, Design of a Novel Heterostructure Photodetectors with Dramatically Enhance Signal-to-Noise based on Resonant Interface-Phonon-Assisted Transitions and Engineering of Energy States to Enhance Transition Rates, 2nd Int'l Conf. and Exhibition on Lasers, Optics & Photonics, Sept. 2014 Philadelphia.

CITED LITERATURE (continued)

[8] M. Stroscio and M. Dutta, Phonons in Nanostructures (Cambridge University Press. 2001).

[9] Lutz, CR; Kanaley, J; Lau, KM; "Intersubband absorption characteristics in OMVPE grown delta-doped GaAs/AlGAs multiple quantum well structures", Journal of Electronic Materials, 29, 225-230 (2000)

[10] C. Edmunds, L. Tang, M. Cervantes, M. Shirazi-HD, J. Shao, A. Grier, A. Valavanis, J. D. Cooper, D. Li, G. Gardner, D. N. Zakharov, Z. Ikoni´c, D. Indjin, P. Harrison, M. J. Manfra, and O. Malis, Phys. Rev. B 88 (2013) 235306

[11] S. Birner, T. Zibold, T. Andlauer, T. Kubis, M. Sabathil, A. Trellakis, P. Vogl, IEEE Trans. Electron Devices 54 (2007) 2137

[12] Michael A. Stroscio, Mikhail V. Kisin, G. Belenky, and Serge Luryi, Phonon enhanced inverse population in asymmetric double quantum wells, Applied Physics Letters (Impact Factor: 3.3). 11/1999; 75(21):3258-3260. DOI: 10.1063/1.125317

[13] Farid, S. et al. 2015. Detection of Interferon gamma using graphene and aptamer based FET-like electrochemical biosensor. Biosensors and Bioelectronics, 71, 294-299.

[14] Gould, H. J., B. J. Sutton, A. J. Beavil, R. L. Beavil, N. McCloskey, H. A. Coker, D. Fear and L. Smurthwaite. 2003. Annu. Rev. Immunol. 21: 579-628.

[15] Iliuk, A. B, L. Hu and W. A. Tao. 2011. Aptamer in bioanalytical applications. Anal. Chem. 83: 4440-4452.

CITED LITERATURE (continued)

[16] Jayasena, S. D. 1999. Aptamers: an emerging class of molecules that rival antibodies in diagnostics. Clin. Chem. 45: 1628-1650.

[17] Mukherjee, S., X. Meshik, M. Choi, S. Farid, D. Datta, Y. Lan, S. Poduri et al. "A Graphene and Aptamer Based Liquid Gated FET-Like Electrochemical Biosensor to Detect Adenosine Triphosphate." IEEE transactions on nanobioscience 14, no. 8 (2015): 967.

[18] Khezrian, S., A. Salimi, H. Teymourian and R. Hallaj. 2013. Label-free electrochemical IgE aptasensor based on covalent attachment of aptamer onto multiwalled carbon nanotubes/ionic liquid/chitosan nanocomposite modified electrode. Biosens. Bioelectron. 43: 218-225.

[19] Maehashi, K., T. Katsura, K. Kerman, Y. Takamura, K. Matsumoto and E. Tamiya. 2007. Label-free protein biosensor based on aptamer-modified carbon nanotube field-effect transistors. Anal. Chem. 79: 782-787.

[20] Meshik, X., K. Xu, M. Dutta and M. A. Stroscio. 2014. Optical detection of lead and potassium ions using a quantum-dot-based aptamer nanosensor. IEEE Trans. Nanobiosci. 13: 161-164.

[21] Ohno, Y., K. Maehashi and K Matsumoto. 2010. Label-free biosensors based on aptamer-modified graphene field-effect transistors. J. Am. Chem. Soc. 132: 18012-18013.

[22] Wang, Z., T. Wilkop, D. Xu, Yi Dong, G. Ma and Q. Cheng. 2007. Surface plasmon resonance imaging for affinity analysis of aptamer-protein interactions with PDMS microfluidic chips. Anal. Bioanal. Chem. 389: 819-825.

CITED LITERATURE (continued)

[23] Wang, Y. Y. and P. J. Burke. 2013. A large-area and contamination-free graphene transistor for liquid-gated sensing applications. Appl. Phys. Lett. 103: 052103

[24] Wu, T.-C., G. Zhao, H. Lu, M. Dutta and M. A. Stroscio. 2013. Quantum-dot-based aptamer beacons for K^+ detection, IEEE Sens. J. 13: 1549-1553.

[25] Wu, Z., F. Zheng, G. Shen and R. Yu. 2009. A hairpin aptamer-based electrochemical biosensing platform for the sensitive detection of proteins. Biomaterials 30: 2950-2955.

[26] Xiao, Y., A. A. Lubin, A. J. Heeger and K. W. Plaxco. 2005. Label-free electronic detection of thrombin in blood serum by using an aptamer-based sensor. Angew. Chem. Int. Ed. 44: 5456-5459.

[27] Xu, D., D. Xu, X. Yu, Z. Liu, W. He and Z. Ma. 2005. Label-free electrochemical detection for aptamer-based array electrodes. Anal. Chem. 777: 5107-5113.

[28] Xu, K., J. Qian and M. A. Stroscio. 2013. Graphene-based molecular sensor based on conformational change of an aptamer, Trans. Elec. Elect. Circuits Syst. 3: 1-5.

[29] Xu, K., et al. 2014. Design and Applications of Nanomaterial-Based and Biomolecule-Based Nanodevices and Nanosensors. In Design and Applications of Nanomaterials for Sensors (pp. 61-97). Springer Netherlands.

CITED LITERATURE (continued)

[30] Xu, K., X. Meshik, B. M. Nichols, E. Zakar, M. Dutta and M. A. Stroscio. 2014. Graphene- and aptamer-based electrochemical biosensor. Nanotechnology 25: 205501.

[31] Xu, K., X. Meshik, B. M. Nichols, E. Zakar, M. Dutta and M. A. Stroscio. 2014. Graphene- and aptamer-based electrochemical biosensor. Nanotechnology 25: 205501.

[32] Farid, S., Mukherjee, S., Sarkar, K., Mazouchi, M., Stroscio, M. A., & Dutta, M. (2016). Enhanced optical properties due to indium incorporation in zinc oxide nanowires. Applied Physics Letters, 108(2), 021106.

[33] Farid, S., Mukherjee, S., Jung, H., Stroscio, M. A., & Dutta, M. (2015). Analysis on the structural, vibrational and defect states of chlorine treated polycrystalline cadmium telluride structures grown by e-beam evaporation.Materials Research Express, 2(2), 025007.

[34] Choi, M. S., Meshik, X., Mukherjee, S., Farid, S., Doan, S., Covnot, L., ... & Stroscio, M. A. (2015). Electrostatic force analysis, optical measurements, and structural characterization of zinc oxide colloidal quantum dots synthesized by sol-gel method. Journal of Applied Physics, 118(19), 194304.

[35] Yi Lan, Chenjie Tang, Junxia (Lucy) Shi, Mitra Dutta, Michael Stroscio. “Phononic properties for enhanced signal-to-noise photodetector.” Computational Electronics (IWCE), 2015 International Workshop

APPENDICES

Appendix A

MATLAB CODE FOR CALCULATING THE ENERGY STATES IN SINGLE-DOUBLE QUANTUM WELL DESIGN WITH GaAlAs MATERIALS

```
%% G.-L. Su, Y. Lan, Aug.14, 2013, all rights reserved
%% Treat GaAs well as zero-potential

clear; clc; close all;
h_bar=1.054571628e-34;
m0=9.10938215e-31;

q=1.602176487e-19;

x1=0.548;
x2=0.259;

dEg1=0.67*1.247*x1;
dEg2=0.67*1.247*x2;

m1=0.067+0.083*x1;
m2=0.067+0.083*x2;
```

Appendix A (Continued)

```
tGaAs=6E-9; %% GaAs well thickness
tb1=6E-9; %% First AlGaAs barrier thickness
tw1=6E-9; %% First AlGaAs well thickness
tb2=0.75E-9; %% Second AlGaAs barrier thickness
tw2=6E-9; %% Second AlGaAs well thickness

PO=[dEg1 0 dEg1 dEg2 dEg1 dEg2 dEg1];
me=[m1 0.067 m1 m2 m1 m2 m1];
t=[20E-9 tGaAs tb1 tw1 tb2 tw2 20E-9];

%% Discretization=0.1nm
dz=0.1E-9;
left(1)=0;
for(m=1:7)
    right(m)=left(m)+t(m);
    left(m+1)=right(m);
end;
V0=ones(1,floor(t(1)/dz))*PO(1);
mass=ones(1,floor(t(1)/dz))*me(1);
z=linspace(left(1)+dz,left(2),floor(t(1)/dz));
for(n=2:7)
    V0=[V0 ones(1,floor(t(n)/dz))*PO(n)];
    mass=[mass ones(1,floor(t(n)/dz))*me(n)];
```

Appendix A (Continued)

```
    z=[z linspace(left(n)+dz,left(n+1),floor(t(n)/dz))];
end;
Npt=length(z);
Figure;
subplot(2,1,1);
plot(z/1E-9,V0,'linewidth',2); xlabel('z (nm)'); ylabel('\Delta E_C (eV)');
grid on;
subplot(2,1,2);
plot(z/1E-9,mass,'linewidth',2); xlabel('z (nm)'); ylabel('Effective Masses
(m_0)');
grid on;

A=(diag(ones(Npt-1,1),1)-diag(ones(Npt-1,1),-1))/2/dz;
T=-(h_bar^2/(2*m0))*A*diag(1./mass)*A;
V=diag(V0)*q;
H=T+V;
%% Solve for 20 solutions
solnum=20;
[V,E]=eigs(H,solnum,'sa');
Figure;
plot(z/1E-9,V0,'linewidth',2); xlabel('z (nm)'); ylabel('Energy (eV)');
hold on;
cc=hsv(solnum/2);
```

Appendix A (Continued)

```
for(m=1:10)
e(m)=E(2*m-1,2*m-1)/q;
    plot(z/1E-9,e(m)*ones(1,length(z)),'linewidth',2,'color',cc(m,:));
end;
legend('\DeltaE_C',...
    strcat('E1=',num2str(e(1)),'eV'),...
    strcat('E2=',num2str(e(2)),'eV'),...
    strcat('E3=',num2str(e(3)),'eV'),...
    strcat('E4=',num2str(e(4)),'eV'),...
    strcat('E5=',num2str(e(5)),'eV'),...
    strcat('E6=',num2str(e(6)),'eV'),...
    strcat('E7=',num2str(e(7)),'eV'),...
    strcat('E8=',num2str(e(8)),'eV'),...
    strcat('E9=',num2str(e(9)),'eV'),...
    strcat('E10=',num2str(e(10)),'eV'));
clear A T H Npt right left dEg1 dEg2 m n solnum tGaAs tb1 tb2 tw1 tw2 cc
```

Appendix B

MATLAB CODE FOR FINDING INTERFACE PHONON MODES IN GaAlAs MATERIAL SYSTEMS

```
d1=6e-9;

d2=12e-9;

d3=18e-9;

d4=18.75e-9;

d5=24.75e-9;


m1=0.548;

m2=0;

m3=0.259;


ac1=10.89-2.73*m1;

ac2=10.89-2.73*m2;

ac3=10.89-2.73*m3;


wloga1=36.25-6.55*m1+1.79*m1^2;

wloga2=36.25-6.55*m2+1.79*m2^2;

wloga3=36.25-6.55*m3+1.79*m3^2;


wloal1=44.63+8.78*m1-3.32*m1^2;
```

Appendix B (Continued)

```
wloal2=44.63+8.78*m2-3.32*m2^2;

wloal3=44.63+8.78*m3-3.32*m3^2;


wtoga1=33.29-0.64*m1-1.16*m1^2;

wtoga2=33.29-0.64*m2-1.16*m2^2;

wtoga3=33.29-0.64*m3-1.16*m3^2;


wtoal1=44.63+0.55*m1-0.30*m1^2;

wtoal2=44.63+0.55*m2-0.30*m2^2;

wtoal3=44.63+0.55*m3-0.30*m3^2;


A=1;

W=linspace(48, 49, 100001);

for(m=1:100001)

w=W(m);

a1=(ac1)*(((w^2-wloga1^2)*(w^2-wloal1^2))/((w^2-wtoga1^2)*(w^2-wtoal1^2)));

a2=(ac2)*(((w^2-wloga2^2)*(w^2-wloal2^2))/((w^2-wtoga2^2)*(w^2-wtoal2^2)));

a3=(ac3)*(((w^2-wloga3^2)*(w^2-wloal3^2))/((w^2-wtoga3^2)*(w^2-wtoal3^2)));


q=10e8;


B=(1/2)*A*(1+(a1/a2));

C=(1/2)*A*(1-(a1/a2));
```

Appendix B (Continued)

```
D=(1/2)*((1+(a2/a1))*B*exp(q*d1)+(1-(a2/a1))*C*exp(-q*d1));

E=(1/2)*((1-(a2/a1))*B*exp(q*d1)+(1+(a2/a1))*C*exp(-q*d1));

F=(1/2)*((1+(a1/a3))*D*exp(q*(d2-d1))+(1-(a1/a3))*E*exp(-q*(d2-d1)));

G=(1/2)*((1-(a1/a3))*D*exp(q*(d2-d1))+(1+(a1/a3))*E*exp(-q*(d2-d1)));

H=(1/2)*((1+(a3/a1))*F*exp(q*(d3-d2))+(1-(a3/a1))*G*exp(-q*(d3-d2)));

I=(1/2)*((1-(a3/a1))*F*exp(q*(d3-d2))+(1+(a3/a1))*G*exp(-q*(d3-d2)));

J=(1/2)*((1+(a1/a3))*H*exp(q*(d4-d3))+(1-(a1/a3))*I*exp(-q*(d4-d3)));

K=(1/2)*((1-(a1/a3))*H*exp(q*(d4-d3))+(1+(a1/a3))*I*exp(-q*(d4-d3)));

L1=J*exp(q*(d5-d4))+K*exp(-q*(d5-d4));


L=1e-9;

h=1.0546e-27;

y(m)=(J*exp(q*(d5-d4))+K*exp(-q*(d5-d4)))/(J*exp(q*(d5-d4))-K*exp(-q*(d5-d4))

)+a3/a1;

end;

Figure;

plot(W,y);


for nloop = 1: length(y)-1

if y(nloop) * y(nloop+1) < 0

fprintf('zero point =%f , \n', W(nloop));

end

end
```

Appendix C

MATLAB CODE FOR SOLVING A FOR CORRESONDING INTERFACE PHONON MODES IN GAALAS SYSTEM

```
A = linspace(-1, 1, 1000001);
%%%%%%%%%%%%%%%%%%%%%%%%%%%%%%%%%%%%%%
%%%% Setup w value to find differential
w=44.78195

%%% w_left and w_right are ought to take ifinitesimal part of w, where
%%% w_right - w_left = delta w; If more precision needed, just increase
%%% variable precision
precision = 10;
w_left = (1 - 1/10^precision) * w;
w_right = (1 + 1/10^precision) * w;
w = [w_left w_right];
clear precision;
%%%%%%%%%%%%%%%%%%%%%%%%%%%%%%%%%%%%%%

d1=6e-9;
d2=12e-9;
d3=18e-9;
d4=18.75e-9;
```

Appendix C (Continued)

```
d5=24.75e-9;

m1=0.548;
m2=0;
m3=0.259;

ac1=10.89-2.73*m1;
ac2=10.89-2.73*m2;
ac3=10.89-2.73*m3;

wloga1=36.25-6.55*m1+1.79*m1^2;
wloga2=36.25-6.55*m2+1.79*m2^2;
wloga3=36.25-6.55*m3+1.79*m3^2;

wloal1=44.63+8.78*m1-3.32*m1^2;
wloal2=44.63+8.78*m2-3.32*m2^2;
wloal3=44.63+8.78*m3-3.32*m3^2;

wtoga1=33.29-0.64*m1-1.16*m1^2;
wtoga2=33.29-0.64*m2-1.16*m2^2;
wtoga3=33.29-0.64*m3-1.16*m3^2;

wtoal1=44.63+0.55*m1-0.30*m1^2;
```

Appendix C (Continued)

```
wtoal2=44.63+0.55*m2-0.30*m2^2;
wtoal3=44.63+0.55*m3-0.30*m3^2;

a1=(ac1)*(((w.^2-wloga1^2).*(w.^2-wloal1^2))./((w.^2-wtoga1^2).*(w.^2-wtoal1^
2)));
a2=(ac2)*(((w.^2-wloga2^2).*(w.^2-wloal2^2))./((w.^2-wtoga2^2).*(w.^2-wtoal2^
2)));
a3=(ac3)*(((w.^2-wloga3^2).*(w.^2-wloal3^2))./((w.^2-wtoga3^2).*(w.^2-wtoal3^
2)));

%%% here x values here shall be a number, NOT array
x1=diff(a1) / diff(w);
x2=diff(a2) / diff(w);
x3=diff(a3) / diff(w);

q=12e8;

B=(1/2)*A*(1+(a1/a2));
C=(1/2)*A*(1-(a1/a2));
D=(1/2)*((1+(a2/a1))*B*exp(q*d1)+(1-(a2/a1))*C*exp(-q*d1));
E=(1/2)*((1-(a2/a1))*B*exp(q*d1)+(1+(a2/a1))*C*exp(-q*d1));
F=(1/2)*((1+(a1/a3))*D*exp(q*(d2-d1))+(1-(a1/a3))*E*exp(-q*(d2-d1)));
G=(1/2)*((1-(a1/a3))*D*exp(q*(d2-d1))+(1+(a1/a3))*E*exp(-q*(d2-d1)));
```

Appendix C (Continued)

```
H=(1/2)*((1+(a3/a1))*F*exp(q*(d3-d2))+(1-(a3/a1))*G*exp(-q*(d3-d2)));

I=(1/2)*((1-(a3/a1))*F*exp(q*(d3-d2))+(1+(a3/a1))*G*exp(-q*(d3-d2)));

J=(1/2)*((1+(a1/a3))*H*exp(q*(d4-d3))+(1-(a1/a3))*I*exp(-q*(d4-d3)));

K=(1/2)*((1-(a1/a3))*H*exp(q*(d4-d3))+(1+(a1/a3))*I*exp(-q*(d4-d3)));

L1=J*exp(q*(d5-d4))+K*exp(-q*(d5-d4));

L=1e-17;

h=1.0546e-27;


y=(J*exp(q*(d5-d4))+K*exp(-q*(d5-d4)))/(J*exp(q*(d5-d4))-K*exp(-q*(d5-d4)))+a
3/a1;


z1=x1*q*(A.^2);

z2=x2*q*((B.^2)*(exp(2*q*d1)-1)-(C.^2)*(exp(-2*q*d1)-1));

z3=x1*q*((D.^2)*(exp(2*q*(d2-d1))-1)-(E.^2)*(exp(-2*q*(d2-d1))-1));

z4=x3*q*((F.^2)*(exp(2*q*(d3-d2))-1)-(G.^2)*(exp(-2*q*(d3-d2))-1));

z5=x1*q*((H.^2)*(exp(2*q*(d4-d3))-1)-(I.^2)*(exp(-2*q*(d4-d3))-1));

z6=x3*q*((J.^2)*(exp(2*q*(d5-d4))-1)-(K.^2)*(exp(-2*q*(d5-d4))-1));

z7=x1*(q)*(L1.^2);


x=4*pi*h/(L^2);

y1=z1+z2+z3+z4+z5+z6+z7-x;


format long
```

Appendix C (Continued)

```
for nloop = 1: length(y1)-1

if y1(nloop) * y1(nloop+1) < 0

fprintf('zero point =%f , \n', A(nloop));

end

end
```

Appendix D

MATLAB CODE FOR PLOTTING PHONON POTENTIAL CURVES ALONG THE Z DIRECTION OF THE STRUCTURE IN GaAlAs SYSTEM

```
%WHEN THE WAVE VECTOR = 6E08 THERE'S 16 INTERFACE PHONON
MODES
a=[0.00000011216 0.001802 0.010052 0.00000100910 0.00000048302 0.000116
0.00007 0.000014 0.00000000254 0.00000006376 0.00000009078 0.00000000082
0.000062 0.000202 0.000368 0.000004];
W=[32.61649 32.68106 32.68169 32.8066 33.64614 34.14489 34.14682 34.59718
44.76119 44.78192 44.78202 44.81387 47.01546 47.58227 47.5847 48.13497];

Figure;
cc=hsv(16);
for i=1:16
A=a(i);
w=W(i);

d1=6e-9;
d2=12e-9;
d3=18e-9;
d4=18.75e-9;
```

Appendix D (Continued)

```
d5=24.75e-9;

m1=0.548;
m2=0;
m3=0.259;

ac1=10.89-2.73*m1;
ac2=10.89-2.73*m2;
ac3=10.89-2.73*m3;

wloga1=36.25-6.55*m1+1.79*m1^2;
wloga2=36.25-6.55*m2+1.79*m2^2;
wloga3=36.25-6.55*m3+1.79*m3^2;

wloal1=44.63+8.78*m1-3.32*m1^2;
wloal2=44.63+8.78*m2-3.32*m2^2;
wloal3=44.63+8.78*m3-3.32*m3^2;

wtoga1=33.29-0.64*m1-1.16*m1^2;
wtoga2=33.29-0.64*m2-1.16*m2^2;
wtoga3=33.29-0.64*m3-1.16*m3^2;

wtoal1=44.63+0.55*m1-0.30*m1^2;
```

Appendix D (Continued)

```
wtoal2=44.63+0.55*m2-0.30*m2^2;

wtoal3=44.63+0.55*m3-0.30*m3^2;


a1=(ac1)*(((w^2-wloga1^2)*(w^2-wloal1^2))/((w^2-wtoga1^2)*(w^2-wtoal1^2)));

a2=(ac2)*(((w^2-wloga2^2)*(w^2-wloal2^2))/((w^2-wtoga2^2)*(w^2-wtoal2^2)));

a3=(ac3)*(((w^2-wloga3^2)*(w^2-wloal3^2))/((w^2-wtoga3^2)*(w^2-wtoal3^2)));


q=6e8;


B=(1/2)*A*(1+(a1/a2));

C=(1/2)*A*(1-(a1/a2));

D=(1/2)*((1+(a2/a1))*B*exp(q*d1)+(1-(a2/a1))*C*exp(-q*d1));

E=(1/2)*((1-(a2/a1))*B*exp(q*d1)+(1+(a2/a1))*C*exp(-q*d1));

F=(1/2)*((1+(a1/a3))*D*exp(q*(d2-d1))+(1-(a1/a3))*E*exp(-q*(d2-d1)));

G=(1/2)*((1-(a1/a3))*D*exp(q*(d2-d1))+(1+(a1/a3))*E*exp(-q*(d2-d1)));

H=(1/2)*((1+(a3/a1))*F*exp(q*(d3-d2))+(1-(a3/a1))*G*exp(-q*(d3-d2)));

I=(1/2)*((1-(a3/a1))*F*exp(q*(d3-d2))+(1+(a3/a1))*G*exp(-q*(d3-d2)));

J=(1/2)*((1+(a1/a3))*H*exp(q*(d4-d3))+(1-(a1/a3))*I*exp(-q*(d4-d3)));

K=(1/2)*((1-(a1/a3))*H*exp(q*(d4-d3))+(1+(a1/a3))*I*exp(-q*(d4-d3)));

L=J*exp(q*(d5-d4))+K*exp(-q*(d5-d4));


z1 = -20e-9:0.005e-9:0;

p1=A*exp(q*z1);
```

Appendix D (Continued)

```
z2 = 0:0.005e-9:d1;

p2=B*exp(q*z2)+C*exp(-q*z2);

z3 = d1:0.005e-9:d2;

p3=D*exp(q*(z3-d1))+E*exp(-q*(z3-d1));

z4 = d2:0.005e-9:d3;

p4=F*exp(q*(z4-d2))+G*exp(-q*(z4-d2));

z5 = d3:0.005e-9:d4;

p5=H*exp(q*(z5-d3))+I*exp(-q*(z5-d3));

z6 = d4:0.005e-9:d5;

p6=J*exp(q*(z6-d4))+K*exp(-q*(z6-d4));

z7 = d5:0.005e-9:45e-9;

p7=L*exp(-q*(z7-d5));


plot([z1*(10^9) z2*(10^9) z3*(10^9) z4*(10^9) z5*(10^9) z6*(10^9) z7*(10^9)],[p1
p2 p3 p4 p5 p6 p7],'color',cc(i,:))
P(i,:)=[p1 p2 p3 p4 p5 p6 p7];
hold on


title('Wave Vector q=6x 10^8 (m^-1)', 'fontsize',20);
xlabel('position (nm)', 'fontsize',20);
ylabel('Phonon Potential (eV-nm)','fontsize', 20);
end;
x=[z1 z2 z3 z4 z5 z6 z7];
```

Appendix D (Continued)

```
legendW=num2str(W');
r=legend([repmat('w=',16,1) legendW repmat(' meV',16,1)]);
set(r,'Fontsize',18);
```

Appendix E

MATLAB CODE FOR ELECTRONIC WAVE FUNCTION SIMULATION

```
%% G-L. Su, Y. Lan, Aug.14, 2013, all rights reserved
%% Use finite difference method and Dirichlet boundary condition
%% to calculate energy levels in certain structures.

%% Treat GaAs well as zero-potential
clear; clc; close all;
h_bar=1.054571628e-34;
m0=9.10938215e-31;
q=1.602176487e-19;

x1=0.548;
x2=0.259;

dEg1=0.67*1.247*x1;
dEg2=0.67*1.247*x2;

m1=0.067+0.083*x1;
m2=0.067+0.083*x2;
```

Appendix E (Continued)

```
tGaAs=6E-9; %% GaAs well thickness
tb1=6E-9; %% First AlGaAs barrier thickness
tw1=6E-9; %% First AlGaAs well thickness
tb2=0.75E-9; %% Second AlGaAs barrier thickness
tw2=6E-9; %% Second AlGaAs well thickness

PO=[dEg1 0 dEg1 dEg2 dEg1 dEg2 dEg1];
me=[m1 0.067 m1 m2 m1 m2 m1];
t=[20E-9 tGaAs tb1 tw1 tb2 tw2 20.25E-9];

%% Discretization=0.1nm
dz=0.1E-9;
left(1)=0;
for(m=1:7)
    right(m)=left(m)+t(m);
    left(m+1)=right(m);
end;
V0=ones(1,floor(t(1)/dz))*PO(1);
mass=ones(1,floor(t(1)/dz))*me(1);
z=linspace(left(1)+dz,left(2),floor(t(1)/dz));
for(n=2:7)
    V0=[V0 ones(1,floor(t(n)/dz))*PO(n)];
    mass=[mass ones(1,floor(t(n)/dz))*me(n)];
```

Appendix E (Continued)

```
    z=[z linspace(left(n)+dz,left(n+1),floor(t(n)/dz))];
end;
% phononpotential(z,left,t);
Npt=length(z);
%Figure;
%subplot(2,1,1);
%plot(z/1E-9,V0,'linewidth',2); xlabel('z (nm)'); ylabel('\Delta E_C (eV)');
%grid on;
%subplot(2,1,2);
%plot(z/1E-9,mass,'linewidth',2); xlabel('z (nm)'); ylabel('Effective Masses (m_0)');
%grid on;

A=(diag(ones(Npt-1,1),1)-diag(ones(Npt-1,1),-1))/2/dz;
T=-(h_bar^2/(2*m0))*A*diag(1./mass)*A;
V=diag(V0)*q;
H=T+V;
%% Solve for 20 solutions
solnum=20;
[V,E]=eigs(H,solnum,'sa');

Figure;
plot(z/1E-9,V0,'linewidth',2); xlabel('z (nm)'); ylabel('Energy (eV)');
hold on;
```

Appendix E (Continued)

```
cc=hsv(solnum/2);
for(m=1:6)
    e(m)=E(2*m-1,2*m-1)/q;
    wavefunction(:,m)=WFmending(z,V(:,2*m-1));
    plot(z/1E-9,e(m)*ones(1,length(z)),'linewidth',2,'color',cc(m,:));
end;
legend('\DeltaE_C',...
    strcat('E1=',num2str(e(1)),'eV'),...
    strcat('E2=',num2str(e(2)),'eV'),...
    strcat('E3=',num2str(e(3)),'eV'),...
    strcat('E4=',num2str(e(4)),'eV'),...
    strcat('E5=',num2str(e(5)),'eV'),...
    strcat('E6=',num2str(e(6)),'eV'));
Figure;
plot(z/1E-9,V0,'linewidth',2); xlabel('z (nm)'); ylabel('Energy (eV)');
hold on;
cc=hsv(solnum/2);
for(m=1:6)
    e(m)=E(2*m-1,2*m-1)/q;

plot(z/1E-9,e(m)*ones(1,length(z))-0.025*(wavefunction(:,m)'/max(abs(wavefunctio
n(:,m))))...
        ,'linewidth',2,'color',cc(m,:));
```

Appendix E (Continued)

```
end;
% clear A T H Npt right left dEg1 dEg2 m n solnum tGaAs tb1 tb2 tw1 tw2 cc
```

PUT ANOTHER MATLAB FILE NAMED “WFmending” IN THE SAME FOLDER

CODES ARE AS FOLLOWING

```
function eigfunc=mending(x,vector)
N=length(vector);
for(n=2:N-1)
    if((abs(vector(n))>abs(vector(n-1)))&&(abs(vector(n))>abs(vector(n+1))))
        peak=n;
        break;
    end;
end;
if((peak/2-floor(peak/2))==0)
    for(n=1:(N-3)/2)
        vector(2*n+1)=0.5*(vector(2*n)+vector(2*n+2));
    end;
else
    for(n=1:(N-1)/2)
        vector(2*n)=0.5*(vector(2*n-1)+vector(2*n+1));
```

Appendix E (Continued)

```
    end;
end;
vector(1)=vector(2); vector(N)=vector(N-1);
temp=trapz(x,abs(vector).^2);
eigfunc=vector/sqrt(temp);
```

Appendix F

MATLAB CODE FOR TRANSFER EFFICIENCY CALCULATING

```
function eigfunc=mending(x,vector)
N=length(vector);
for(n=2:N-1)
    if((abs(vector(n))>abs(vector(n-1)))&&(abs(vector(n))>abs(vector(n+1))))
        peak=n;
        break;
    end;
end;
if((peak/2-floor(peak/2))==0)
    for(n=1:(N-3)/2)
        vector(2*n+1)=0.5*(vector(2*n)+vector(2*n+2));
    end;
else
    for(n=1:(N-1)/2)
        vector(2*n)=0.5*(vector(2*n-1)+vector(2*n+1));
    end;
end;
vector(1)=vector(2); vector(N)=vector(N-1);
temp=trapz(x,abs(vector).^2);
```

Appendix F (Continued)

```
eigfunc=vector/sqrt(temp);




% Run QW program first
% Then run phonon program
% Make sure their x axes are the same. this program assumes the phonon program
gives a
% denser x axis.


zz=z-20E-9;
wf2=spline(zz,wavefunction(:,3),x);
wf3=spline(zz,wavefunction(:,2),x);
dx=x(2)-x(1);


for(m=1:size(P,1))
    overlap(m)=sum(abs(wf2.*P(m,:).*wf3))*dx;
end;
figure; plot(overlap,'.-')
```

Appendix G

PERMISSION OF REPRINT OF COPYRIGHTED MATERIALS FROM IEEE

Requirements to be followed when using any portion (e.g., figure, graph, table, or textual material) of an IEEE copyrighted paper in a thesis:

1) In the case of textual material (e.g., using short quotes or referring to the work within these papers) users must give full credit to the original source (author, paper, publication) followed by the IEEE copyright line © 2011 IEEE.
2) In the case of illustrations or tabular material, we require that the copyright line © [Year of original publication] IEEE appear prominently with each reprinted figure and/or table.
3) If a substantial portion of the original paper is to be used, and if you are not the senior author, also obtain the senior author's approval.

Requirements to be followed when using an entire IEEE copyrighted paper in a thesis:

1) The following IEEE copyright/ credit notice should be placed prominently in the references: © [year of original publication] IEEE. Reprinted, with permission, from [author names, paper title, IEEE publication title, and month/year of publication]
2) Only the accepted version of an IEEE copyrighted paper can be used when posting the paper or your thesis on-line.

Appendix G (Continued)

3) In placing the thesis on the author's university website, please display the following message in a prominent place on the website: In reference to IEEE copyrighted material which is used with permission in this thesis, the IEEE does not endorse any of [university/educational entity's name goes here]'s products or services. Internal or personal use of this material is permitted. If interested in reprinting/republishing IEEE copyrighted material for advertising or promotional purposes or for creating new collective works for resale or redistribution, please go tohttp://www.ieee.org/publications_standards/publications/rights/rights_link.html to learn how to obtain a License from RightsLink.

If applicable, University Microfilms and/or ProQuest Library, or the Archives of Canada may supply single copies of the dissertation.

VITA

NAME:	Yi Lan
EDUCATION:	B.A., Material Science Engineering, National Tsing Hua University, 2011
	Ph.D., Electrical and Computer Engineering, University of Illinois at Chicago, 2016
TEACHING ASSISTANT:	Department of ECE, University of Illinois at Chicago, 2011-2016
	High School Physics, Chemistry, and Math, Kaohsiung Howard Cram School, 2017-2010
RESEARCH ASSISTANT:	Nano Engineering Research Group - Michael A. Stroscio Research Group, University of Illinois at Chicago, 2011-2016
	Industrial Technology Research Institute in Hsinchu, Taiwan, 2008
HONOR:	2011-2012 ECE Wexler Scholar Award
PUBLICATIONS:	Yi Lan, Chenjie Tang, Junxia (Lucy) Shi, Mitra Dutta, Michael Stroscio. "Phononic properties for enhanced signal-to-noise photodetector." Computational Electronics (IWCE), 2015 International Workshop
	Yi Lan, Nanzhu Zhang, J. L. Shi, M. Dutta, M. A. Stroscio, Design of a Novel Heterostructure Photodetectors with Dramatically Enhance Signal-toNoise based on Resonant Interface-Phonon-Assisted Transitions and Engineering of Energy States to Enhance Transition Rates, 2nd Int'l Conf. and Exhibition on Lasers, Optics & Photonics, Sept. 2014 Philadelphia.